

Control of flux by narrow passages and hidden targets in cellular biology

This content has been downloaded from IOPscience. Please scroll down to see the full text.

2013 Rep. Prog. Phys. 76 074601

(<http://iopscience.iop.org/0034-4885/76/7/074601>)

View [the table of contents for this issue](#), or go to the [journal homepage](#) for more

Download details:

IP Address: 132.239.1.231

This content was downloaded on 05/02/2014 at 01:39

Please note that [terms and conditions apply](#).

Control of flux by narrow passages and hidden targets in cellular biology

D Holcman¹ and Z Schuss²

¹ Group of Applied Mathematics and Computational Biology, IBENS, Ecole Normale Supérieure, 46 rue d'Ulm 75005 Paris, France

² Department of Mathematics, Tel-Aviv University, Tel-Aviv 69978, Israel

E-mail: david.holcman@ens.fr and schuss@post.tau.ac.il

Received 12 June 2012, in final form 2 April 2013

Published 20 June 2013

Online at stacks.iop.org/RoPP/76/074601

Abstract

Critical biological processes, such as synaptic plasticity and transmission, activation of genes by transcription factors, or double-strained DNA break repair, are controlled by diffusion in structures that have both large and small spatial scales. These may be small binding sites inside or on the surface of the cell, or narrow passages between subcellular compartments. The great disparity in spatial scales is the key to controlling cell function by structure. We report here recent progress on resolving analytical and numerical difficulties in extracting properties from experimental data, from biophysical models, and from Brownian dynamics simulations of diffusion in multi-scale structures. This progress is achieved by developing an analytical approximation methodology for solving the model equations. The reported results are applied to analysis and simulations of subcellular processes and to the quantification of their biological functions.

(Some figures may appear in colour only in the online journal)

Contents

1. Introduction	1	5.5. Regulation of calcium flux through the dendritic spine neck	13
2. From molecular to cellular description	3	5.6. Delivery of vesicles in neurite outgrowth	14
2.1. Flux through narrow passages identifies cellular compartments	4	5.7. DNA repair in a two-dimensional confined chromatin structure	14
2.2. Equation for the MFPT	4	5.8. Hidden binding sites control chemical reactions	15
3. Geometrical classification of cellular domains	6	5.9. Asymmetric dumbbell-shaped division in cell	15
4. The formula for the NET $\bar{\tau}$	7	6. Summary and discussion	16
4.1. Formulae for two-dimensional domains	7	Acknowledgment	17
4.2. Formulae for $\bar{\tau}$ in three-dimensional domains	9	A.1. Derivation of the asymptotic formula for the NET	17
5. Applications to cellular biology and simulations	9	A.2. The Helmholtz integral equation	17
5.1. Applications to Brownian dynamics simulations	9	A.3. Asymptotics by conformal mapping	18
5.2. Synaptic transmission and the synaptic cleft	10	References	19
5.3. Diffusion on a membrane crowded with obstacles	10		
5.4. Stochastic chemical reactions in microdomains	11		

1. Introduction

The great disparity between spatial scales in a biological cell structure leads to time-scale separation between molecular events in the cell and in its physiological response.

Specifically, the time scale of diffusion at large is much shorter than that of diffusing into small and hidden targets in cells. This separation indicates that the conversion of molecular events into cellular response, which is a rare event (on the time scale of diffusion), is controlled by structure. It is well known in the

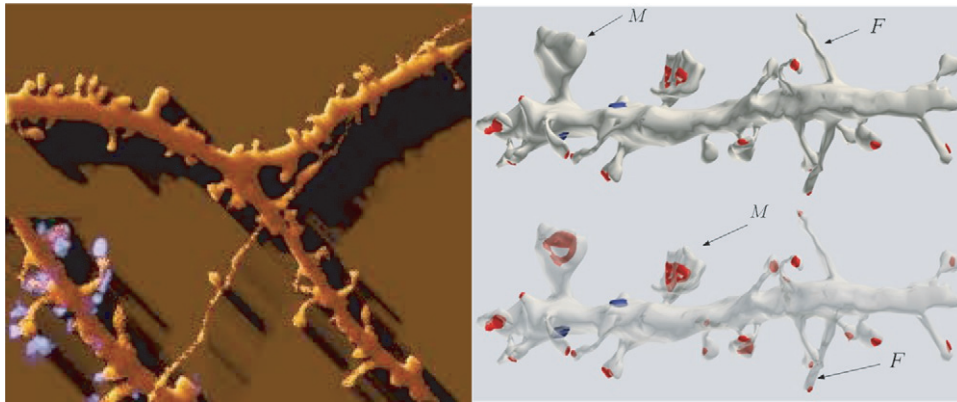


Figure 1. Left: Spines on a dendrite. Right: three-dimensional EM reconstruction of two dendrites from the hippocampus. The PSDs of excitatory synapses are marked red and of inhibitory synapses—blue. Filopodia (marked *F*) and mushroom spines (marked *M*) are clearly seen [9].

theory of ionic channels that structure is the main determinant of channel selectivity and gating [1] (see also MacKinnon Nobel lecture [2]). Traditionally, when the crystallographic structure of a channel is unknown, recordings of channel current–voltage characteristics are used to reconstruct the spatial organization of protein and ions that define the channel pore [3,4]. But even when the crystallographic structure of a channel is known, the determination of the function of different channel components such as gating, ionic selectivity and channel conductances from the molecular structure is only partially known [5]. A possible approach for an answer relies on either solving the Poisson–Nernst–Planck equations [6] or Brownian or molecular dynamics simulations of the joint diffusive motion of protein and ions as well as the computation of the time-dependent electric field (see, for example, [7]).

The resolution of the structure–function relationship in channels is more accurate than in cells due to the nanoscale resolution of channel structure. The coarser scale of structural resolution of cellular and subcellular compartments necessitates perforce much coarser mathematical and biophysical models than channel models. The former can be expected to give much coarser functional information on cellular function than the latter for channel function. In order to produce manageable cell models many physical features have to be given up, for example, interactions between mobile particles, which are the determinants of channel conductance and selectivity. Also the structural model of the cell, which is by and large unknown, has to be simplified. The functional information that can be extracted from the simplified models of cell structure calls for different analytical and simulation tools than in channels. To address the structure–function question in cell models, we focus on several examples of simplified structures of cellular microdomains, such as the structure of enzymatic active sites, confined chromatin structure, the transient structure during cell division and the flow of genetic materials exchanged by diffusion, and in particular on the regulation of diffusion flux in synapses and dendritic spines of neurons, whose spatial structure has been extensively studied [8,9].

There are about 10^{11} neurons in the human brain, each containing about 10^3 synapses, which consist of pre- and postsynaptic terminals. In excitatory connections the latter can

be a dendritic spine-like structure (figure 1). There are also stand-alone spines that all in all can number about 10^5 in a hippocampal neuron. The function of synapses and dendritic spines is still unclear, though their morphological changes in cognitive pathology, such as in epilepsy and autism spectrum disorders, indicate that they may be involved in regulating the synaptic function. The structure–function approach in modeling and analyzing these structures can possibly be the key to bridging the gap between the molecular and the cellular scales.

Recognized more than one hundred years ago by Ramón y Cajal, dendritic spines are small terminal protrusions on neuronal dendrites and are considered to be the main locus of excitatory synaptic connections. The general spine geometry, as observed in figure 1 (right), consists of a relatively narrow cylindrical neck connected to a bulky head (the round part in the schematic figure 4). In fact, spine shapes can fall into one of these categories. In addition, spine geometrical shapes correlate with their physiological functions [8–12]. Interestingly, serial electron microscopy and three-dimensional reconstruction of dendritic spines from Purkinje spiny branchlets of normal adult rats relate spine geometry to synaptic efficacy (figure 2) [8]. Change in spine morphology can be induced by synaptic potentiation protocols [13–15] and indeed, intracellular signaling, such as calcium release from stores, alters the morphology of dendritic spines in cultured hippocampal neurons. These changes in geometry can affect the spine–dendrite communication. One of the first quantitative assessments of geometry was obtained by a direct measurement [16] of diffusion through the spine neck. Concentration gradients between spines and shafts in rat CA1 pyramidal neurons were established by photo-bleaching and photo-release of fluorescein dextran in order to track the time course of re-equilibration. It was well approximated by a single exponential decay, with a time constant in the range 20–100 ms. The role of the spine neck was further investigated experimentally with flash photolysis of caged calcium [10,17] and theoretically in [18], with the main conclusion that geometrical changes in the spine neck, such as the length or the radius, are key modulators of calcium dynamics in the process of spine–dendrite communication [19–21].

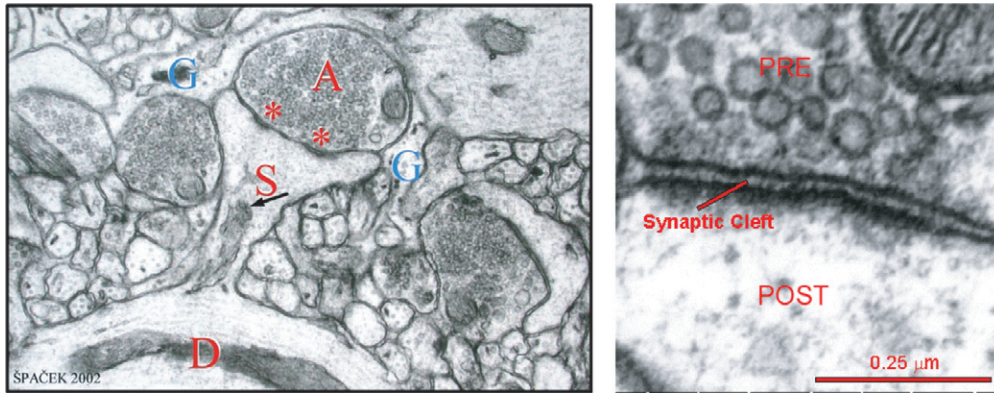


Figure 2. Left: Electron microscopy of an excitatory synapse. Vesicles containing NT can be seen inside the pre-synaptic terminal (marked A). The spine (marked S) is connected to the dendritic shaft (marked D) by a neck. The synaptic cleft separating pre- and post-synaptic membranes is 20–25 nm wide. Glia cells surrounding the synaptic cleft are marked G. The arrow points at organelles inside the spine. Right: blowup of the synaptic cleft vicinity. The synaptic cleft is 20–25 nm wide. Vesicles with NT molecules are clearly seen in this enlargement.

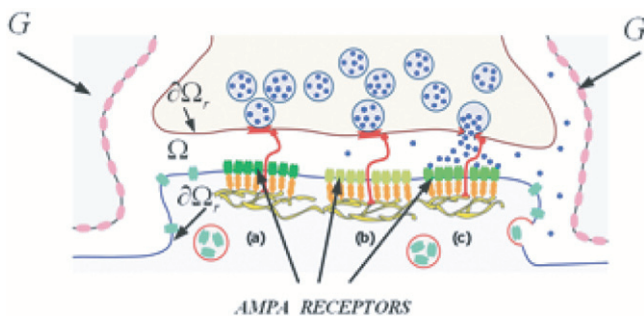


Figure 3. Schematic diagram of the synaptic cleft. The cleft domain is marked Ω . The pre- and post-synaptic membranes are reflecting boundaries ($\partial\Omega_r$) for the Brownian trajectories of the NT molecules (blue dots). The glia cells G and the AMPARs form the absorbing boundary $\partial\Omega_a$. Clusters of AMPARs (a,b,c) are co-localized with release sites of vesicle fusion, mediated by adhesion molecules (red).

The connection between the head and the neck is not only relevant to three-dimensional diffusion in the bulk, but also for two-dimensional surface diffusion. In fact, synaptic transmission and plasticity involve the trafficking of receptors on cell membranes [22–27], such as AMPA or NMDA glutamatergic receptors, which mediate the post-synaptic current (figure 3). The number and type of receptors that shape the synaptic current [23] could be regulated by spine geometry. Regulation of synaptic current by spine geometry was explored theoretically using asymptotic expressions for the residence time [28, 29], and experimentally by monitoring the motion of AMPA receptors on the surface of mature neurons [30]. A recent review of early results on the NET problem with many biological applications is given in [31].

2. From molecular to cellular description

In this review, we describe how to bridge between physical models at the molecular scale and the micrometer scale, at which cells filter and convert molecular signals into cellular response. The latter defines cellular or subcellular function. We report here recent progress in quantifying analytically the

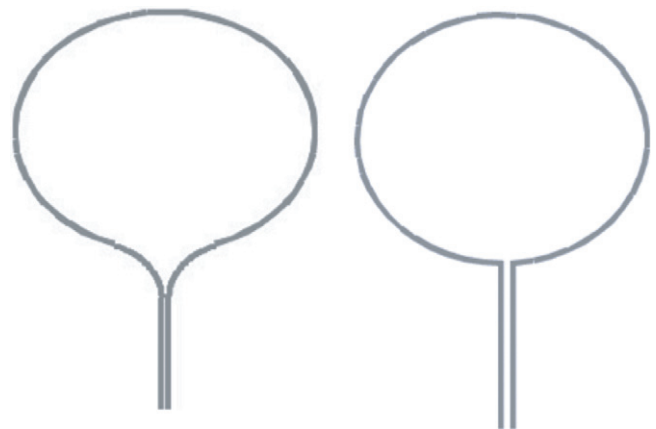


Figure 4. Schematic diagram of a dendritic spine with a smoothly connected neck (left) and with a neck connected at a finite angle (right).

control of diffusion flux into small absorbing targets or through narrow passages in cells. This case is especially important in molecular searches that are not directed at long distances by a field of force and the only flux control mechanism is the geometrical structure. We discuss specific applications of the flux formulae in dendritic spines, in the case of synaptic transmission, for enzyme structure and hidden target sites, for diffusion in the confined chromatin structure in the context of DNA repair, and the unilateral flow of genetic materials exchanged by diffusion during cell division.

The behavior of molecules is complex not only because of their individual structure, but also because they form clusters, interact, reflect and so on. At this stage we only have access to certain sampled molecular trajectories, thus it is unclear how to reconstruct their dynamics from the statistics of the samples. In order to interpret molecular data, we adopt the widely accepted model of molecular motion as diffusion in a field of force. The force field may represent electric interactions with fixed or mobile charges, dielectric interactions with obstacles, such as lipid bilayers and other fixed cell components, hydrodynamical interactions with an ambient flow field, and so on. The task of molecular-level model is to extract cellular level properties and infer from it cell function.

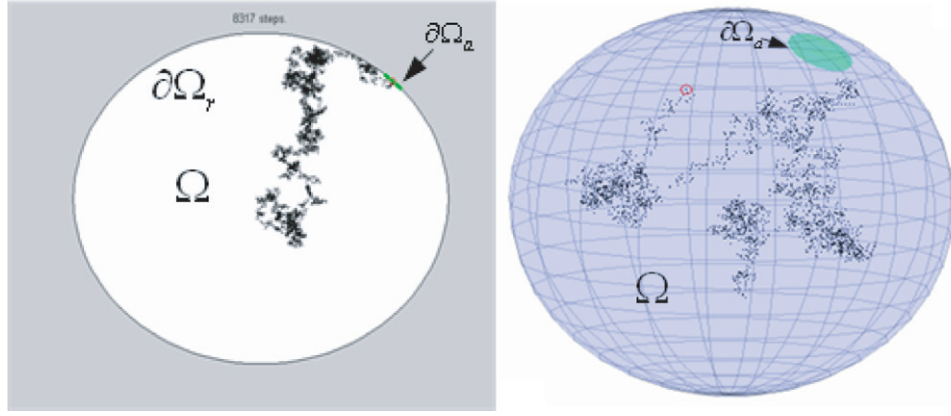


Figure 5. Left: Brownian motion in a circular disk whose boundary is reflecting, except for a short absorbing arc $\partial\Omega_a$ (marked green). Right: Brownian motion on the surface of a decapitated sphere. The circumference of the spherical cap (marked green) is the absorbing boundary $\partial\Omega_a$.

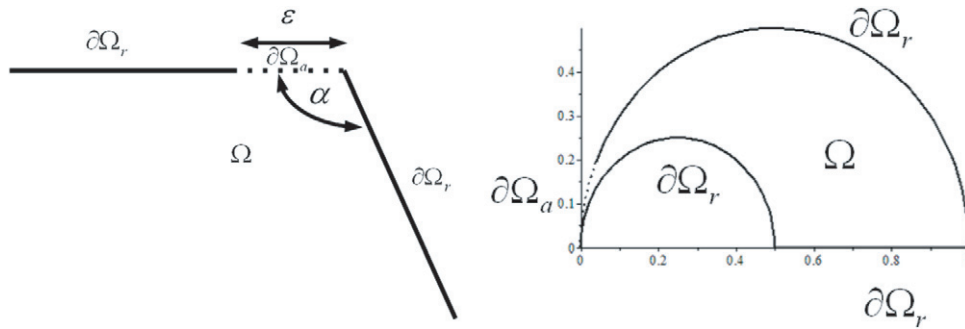


Figure 6. Left: the domain Ω is on one side of the angular sector, the solid lines form the reflecting boundary $\partial\Omega_r$, and the dotted segment of length ε is the absorbing boundary $\partial\Omega_a$. Right: the domain Ω is enclosed between two tangent circular arcs and the x -axis, which form the reflecting boundary $\partial\Omega_r$, except for a short arc $\partial\Omega_a$ of length ε , which is absorbing.

2.1. Flux through narrow passages identifies cellular compartments

The random movement of ions, proteins and other particles in cells is traditionally described as Brownian motion, as mentioned above. The Brownian trajectories are reflected at the cell membrane and at other obstacles, but can be absorbed (terminated) at receptors and other binding sites or when they exit the cell (or a subcellular compartment) and enter another structure. Different compartments for Brownian trajectories are defined here by the probability density of the trajectories or the statistics of the time a trajectory spends at a point. As in segmentation of images (or other data, see Wikipedia), a histogram is computed from all points visited by a trajectory (or trajectories) and the peaks and valleys in the histogram are used to identify the compartments as clusters. What makes the clusters, be it membranes, obstacles, or forces, is an active field of experimental live cell imaging by super-resolution microscopy [32, 33]. By its very definition, the passage of a trajectory from one compartment to the other is a rare event. The rare events may be thermal activation over a potential barrier and/or traversing a narrow passage, such as a channel, a nano-pore, or a narrow neck.

The mean first passage time (MFPT) $\bar{\tau}$ of a Brownian trajectory from a compartment to an absorbing target or through a narrow passage is a fundamental concept in the description of rare events. Specifically, the probability density

function of the time spent in a compartment prior to termination or escape from the compartment in the limit of small target is exponential for sufficiently long times,

$$p_{\bar{\tau}}(t) \sim \bar{\tau}^{-1} \exp\{-t/\bar{\tau}\}. \quad (1)$$

The exponential rate $\bar{\tau}^{-1}$ is therefore the flux into the absorbing target. In the case of crossing from one compartment to another through a narrow neck the crossing rate is $1/2\bar{\tau}$, where $\bar{\tau}$ is the MFPT to the stochastic separatrix (SS) between the compartments. The latter is the locus of initial points of a Brownian trajectory from which it ends up in one compartment or the other with equal probabilities [34].

2.2. Equation for the MFPT

We consider a compartment Ω whose boundary $\partial\Omega$ consists of a part $\partial\Omega_r$ that reflects Brownian trajectories, e.g. a cell membrane, and a small part $\partial\Omega_a$ that absorbs them (see figures 5–11). The MFPT $\bar{\tau}$ depends on the starting point x of the Brownian trajectory, thus it should be denoted $\bar{\tau}(x)$. This function is the solution of the classical mixed Neumann–Dirichlet boundary value problem for the Laplace equation [35–37],

$$D\nabla^2 \bar{\tau}(x) = -1 \quad \text{for } x \in \Omega \quad (2)$$

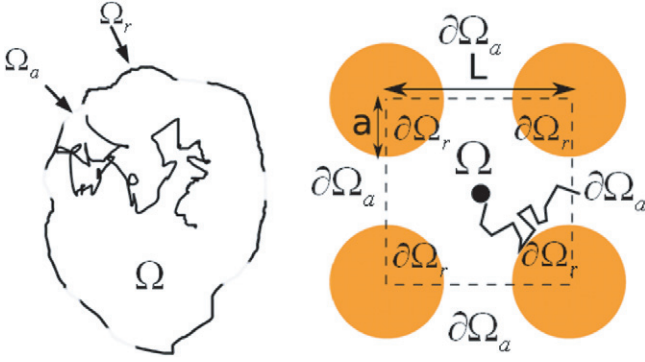


Figure 7. Brownian trajectory inside a compartment containing well-separated absorbing windows. Left: the reflecting boundary $\partial\Omega_r$ consists of arcs and the absorbing boundary $\partial\Omega_a$ consists of well-separated small absorbing windows. Right: the domain Ω is the white area inside the dashed square. The absorbing boundary $\partial\Omega_a$ consists of the four segments of length L . The reflecting boundary $\partial\Omega_r$ consists of the four arcs of the orange disks.

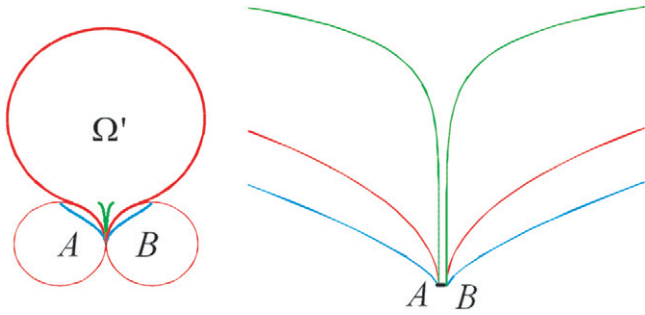


Figure 8. Left: the planar domain Ω' is bounded by a large circular arc connected smoothly to a funnel formed by moving ε apart two tangent circular arcs of radius R_c (i.e. $AB = \varepsilon$). Right: blowup of the cusp region. The red, green and blue necks correspond to $\nu = 1, 0.4$ and 5 in (19), respectively.

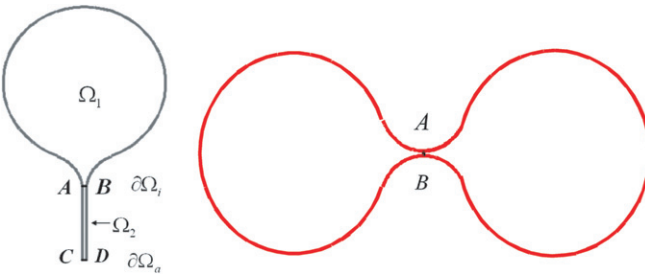


Figure 9. Left: a composite domain consists of a bulky head Ω_1 connected by a funnel to a narrow neck Ω_2 at an interface $\partial\Omega_i = AB$. The entire boundary is reflecting for Brownian motion, except for a small absorbing window $\partial\Omega_a$ at the end CD of the neck Ω_2 . Right: a dumbbell-shaped domain consists of two large compartments Ω_1 and Ω_3 connected by a narrow neck Ω_2 . The bottleneck is the interval AB .

$$\frac{\partial \bar{\tau}(x)}{\partial n} = 0 \quad \text{for } x \in \partial\Omega_r \quad (3)$$

$$\bar{\tau}(x) = 0 \quad \text{for } x \in \partial\Omega_a, \quad (4)$$

where D is the diffusion coefficient and \mathbf{n} is the unit outer normal to the boundary [37]. The system (2)–(4) follows from the backward Kolmogorov equation [37] (the adjoint of the

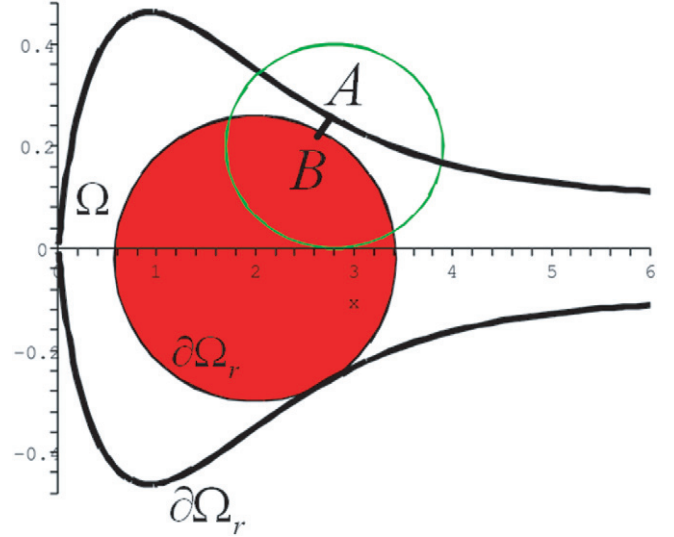


Figure 10. The domain Ω is enclosed between the black curve, the red obstacle, and the segment AB . The reflecting boundary $\partial\Omega_r$ consists of the curve and the boundary of the obstacle. The absorbing boundary $\partial\Omega_a$ is the segment AB .

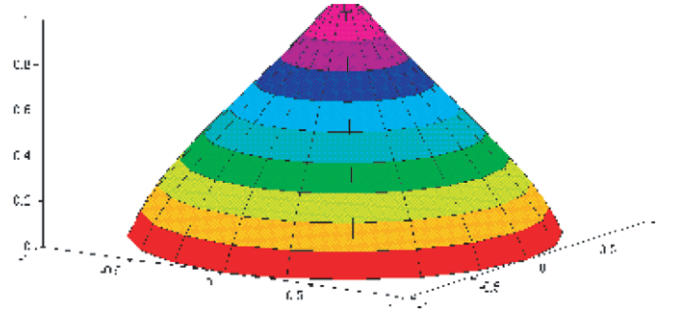


Figure 11. $\partial\Omega_a$ is an opening at the end of a funnel of finite angle (see figure 8 (right)).

Fokker–Planck equation) for the transition probability density function $p(\mathbf{y}, t | \mathbf{x})$ of the Brownian trajectories,

$$\frac{\partial p(\mathbf{y}, t | \mathbf{x})}{\partial t} = D \nabla_x^2 p(\mathbf{y}, t | \mathbf{x}) \quad \text{for } \mathbf{x}, \mathbf{y} \in \Omega \quad (5)$$

$$\frac{\partial p(\mathbf{y}, t | \mathbf{x})}{\partial n_x} = 0 \quad \text{for } \mathbf{y} \in \Omega, \quad \mathbf{x} \in \partial\Omega_r \quad (6)$$

$$p(\mathbf{y}, t | \mathbf{x}) = 0 \quad \text{for } \mathbf{y} \in \Omega, \quad \mathbf{x} \in \partial\Omega_a \quad (7)$$

$$p(\mathbf{y}, 0 | \mathbf{x}) = \delta(\mathbf{y} - \mathbf{x}) \quad \text{for } \mathbf{x}, \mathbf{y} \in \Omega. \quad (8)$$

The survival probability of Brownian trajectories that start at $\mathbf{x} \in \Omega$ is

$$\Pr\{\tau > t | \mathbf{x}\} = \int_{\Omega} p(\mathbf{y}, t | \mathbf{x}) d\mathbf{y} \quad (9)$$

and its mean value is

$$\bar{\tau}(\mathbf{x}) = \int_0^{\infty} \Pr\{\tau > t | \mathbf{x}\} dt. \quad (10)$$

It follows that

$$\begin{aligned} D \nabla^2 \bar{\tau}(\mathbf{x}) &= \int_0^{\infty} D \nabla_x^2 \Pr\{\tau > t | \mathbf{x}\} dt \\ &= \int_0^{\infty} \int_{\Omega} \frac{\partial p(\mathbf{y}, t | \mathbf{x})}{\partial t} d\mathbf{y} dt = -1. \end{aligned} \quad (11)$$

The last equality in (11) follows from the initial condition (8) and the Neumann and Dirichlet conditions (3) and (4) are inherited from (6) and (7), respectively.

No explicit solutions to the problem (2)–(4) are known in general. If the absorbing part of the boundary $\partial\Omega_a$ is much smaller than the entire boundary $\partial\Omega$, numerical solutions to the problem are very hard to construct due to the presence of a boundary layer near $\partial\Omega_a$, where gradients are very large so the numerical complexity becomes prohibitive. The problem cannot be circumvented by Brownian dynamics simulations of the MFPT $\bar{\tau}$, because reaching $\partial\Omega_a$ is a rare event on the time scale of diffusion. The remedy to these difficulties is the construction of analytical approximations to the solution of (2)–(4) by new asymptotic methods developed specifically for the problem at hand.

3. Geometrical classification of cellular domains

The resolution of function from structure relies on the geometrical properties of the structure. Specifically, the geometry of small targets and narrow passages is the determinant of the diffusion influx and efflux of ions and molecules in cellular compartments or on cellular membranes. These can be determined analytically by calculating the MFPT of two- and three-dimensional Brownian trajectories from compartments to small targets.

The MFPT of two-dimensional Brownian motion on a membrane surface is described by a two-dimensional version of the boundary value problem (2)–(4) with the Laplace–Beltrami rather than the Laplace operator (see Wikipedia). The boundary of a surface compartment consists of a curve that reflects Brownian trajectories on the surface and a small absorbing curve at which trajectories are terminated. The domain can be represented in parameter space as a planar domain Ω whose boundary $\partial\Omega$ consists of a reflecting curve $\partial\Omega_r$ and a short absorbing curve $\partial\Omega_a$ (figure 5). The small window $\partial\Omega_a$ studied here can be classified as follows:

- (i) $\partial\Omega_a$ is a short part of the smooth boundary curve $\partial\Omega$ (figure 5 (left)).
- (ii) $\partial\Omega_a$ can be placed at a corner or a cusp (figure 6).
- (iii) $\partial\Omega_a$ can be placed at the end of a cusp-shaped funnel of the boundary (figures 7 (right), 8 (left), or 9, or the surface of revolution obtained by rotating it about its axis of symmetry).
- (iv) The compartment Ω can consist of a bulky head connected to an essentially one-dimensional cylinder of small radius a and length L , as is the case of a neuronal spine membrane (see figure 9 (left)).
- (v) More complicated structures are formed by joining two or more bulky heads by short or long narrow strips or cylinders (dumbbell-shaped domains, see figure 9 (right)). The former can be formed on a spine membrane that contains closely bunched obstacles, such as pickets, fences, non-interacting molecules, actin filaments, and so on, between which a diffusing receptor has to squeeze on its way to the post-synaptic density (figure 7). In this case the effective motion of the diffusing receptor is dominated by the mean time $\bar{\tau}$ to squeeze through the narrow straits formed by the obstacles (see section 5.3).

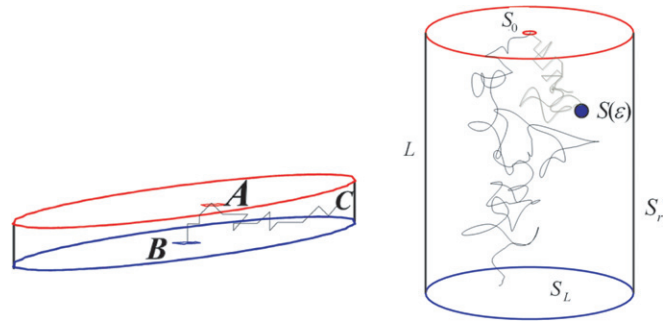


Figure 12. Left: a schematic model of the synaptic cleft 2 (right) and 3. Right: a schematic model of the spine neck (figure 3 (left) and $\partial\Omega_2$ in figure 9 (left)). A Brownian trajectory enters a cylindrical neck (e.g. of a neuronal spine) at a source S_0 and can leak through a small window $S(\varepsilon)$ (e.g. a pump) or reach the absorbing bottom (e.g. the dendritic shaft).

- (vi) A collection of well-separated windows (figure 7).

In the context of the above classification, we define the following categories of narrow escape problems for solid structures with a small absorbing window $\partial\Omega_a$:

- (i) $\partial\Omega_a$ is a circular disk on a regular boundary $\partial\Omega$ (figure 5 (right) of a decapitated ball with an absorbing disk (marked green)).
- (ii) $\partial\Omega_a$ is a disk at the end of a funnel (e.g. obtained by rotating figure 8 about its axis of symmetry).
- (iii) $\partial\Omega_a$ is a disk at the end of a narrow cylindrical neck (e.g. obtained by rotating figure 9 (left) about its axis of symmetry).
- (iv) In dumbbell-shaped structure, obtained by rotating figure 9 (right) about its axis of symmetry, the middle surface is a small target. A key quantification is given by the principal eigenvalue of the Laplace equation.
- (v) Leakage through a small window in a structure that conducts Brownian particles from a source to a relatively large absorbing part of the boundary and the particles can leak out through small absorbing windows in the reflecting part of the boundary. This is the case, for example, of the synaptic cleft that conducts neurotransmitter molecules, released from a vesicle at the pre-synaptic terminal, either to receptors in the post-synaptic distribution on the spine membrane or to the surrounding glia cells (figure 12 (left)). The structure of the cleft is approximately a short cylinder with a source of Brownian particles in one of the impermeable bases, small absorbing windows in the other impermeable base, and absorbing lateral envelop. Another example is that of calcium leakage through channels in the spine neck that conducts calcium to the absorbing end at the dendrite (figure 12 (right)).
- (vi) $\partial\Omega_a$ consists of a number of well-separated absorbing windows (figure 7 (left)). The absorbing windows can be at a regular boundary (figure 5 (right)) or at the ends of funnels (figure 9 (left) with several necks).

The MFPT to the small absorbing target or through the narrow neck depends strongly on the detailed geometrical features of the listed types of compartments and their connections to necks. Differences of orders of magnitude in the MFPTs

through a neck can arise between necks connected to the head at an angle or smoothly by a funnel. The local curvature of the connection can change $\bar{\tau}$ by orders of magnitude.

4. The formula for the NET $\bar{\tau}$

The analytical expression for the MFPT $\bar{\tau}$ strongly depends on the geometrical features of the compartment. It thereby defines time scales of diffusion influx (respectively efflux) to (respectively from) the compartment, which can be interpreted as regulation of the flux. Thus the analytical asymptotic approximation to $\bar{\tau}$ expresses the influence of geometrical structure on cellular functions that consist in controlling diffusion fluxes.

The asymptotic formulae for $\bar{\tau}$ can be classified according to the local geometry of the compartment near the absorbing sites or narrow passages, which are the main controllers of the diffusion flux. Obviously, the formulae in two-dimensional compartments are different than in three-dimensional ones.

4.1. Formulae for two-dimensional domains

The MFPT from a domain Ω in the plane to a small sub-arc $\partial\Omega_a$ (of length a) of the boundary $\partial\Omega$, according to the classification in section 3, is given by the following.

- (i) For type (I) ($\partial\Omega_a$ is a sub-arc of a smooth boundary figure 5 (left)) the MFPT from any point x in Ω to $\partial\Omega_a$ is denoted $\bar{\tau}_{x \rightarrow \partial\Omega_a}$. This is due to the fact that for

$$\varepsilon = \frac{\pi |\partial\Omega_a|}{|\partial\Omega|} = \frac{\pi a}{|\partial\Omega|} \ll 1 \quad (12)$$

the MFPT is independent of x outside a small vicinity of $\partial\Omega_a$ (called a boundary layer). Thus for $x \in \Omega$, outside a boundary layer near $\partial\Omega_a$,

$$\bar{\tau}_{x \rightarrow \partial\Omega_a} = \frac{|\Omega|}{\pi D} \ln \frac{1}{\varepsilon} + O(1), \quad (13)$$

where $O(1)$ depends on the initial distribution of x [38–50]. In particular, if Ω is a disk of radius R , then for x at the center of the disk,

$$\bar{\tau}_{x \rightarrow \partial\Omega_a} = \frac{R^2}{D} \left[\log \frac{R}{a} + 2 \log 2 + \frac{1}{4} + O(\varepsilon) \right],$$

and averaging with respect to a uniform distribution of x in the disk [45]

$$\bar{\tau} = \frac{R^2}{D} \left[\log \frac{R}{a} + 2 \log 2 + \frac{1}{8} + O(\varepsilon) \right].$$

Formula (13) indicates that the flux through a hole in a smooth wall on a flat membrane surface (e.g. a corral) is regulated by the following parameters, the area $|\Omega|$ inside the wall, the diffusion coefficient D , and the aspect ratio ε (12).

In the case of Brownian motion on a sphere of radius R the MFPT to an absorbing circle centered on the north-south

axis near the south pole with small radius $a = R \sin \delta/2$ (figure 5 (right)) is given by

$$\bar{\tau} = \frac{2R^2}{D} \log \frac{\sin \frac{\theta}{2}}{\sin \frac{\delta}{2}}, \quad (14)$$

where θ is the angle between x and the south–north axis of the sphere [46–51].

- (ii) For type (II), if the absorbing window is located at a corner of angle α (figure 6 (left)), then

$$\bar{\tau} = \frac{|\Omega|_g}{D\alpha} \left[\log \frac{1}{\varepsilon} + O(1) \right], \quad (15)$$

where $|\Omega|_g$ is the surface area of the domain on the curved surface, calculated according to the Riemannian metric on the surface [46]. Formula (15) indicates that control of flux is also regulated by the access to the absorbing window afforded by the angle of the corner leading to the window (see figure 6 (left)).

- (iii) For type (III), if the absorbing window is located at a cusp (figure 6 (right)), then $\bar{\tau}$ grows algebraically, rather than logarithmically. Thus, in the domain bounded between two tangent circles, the expected lifetime is

$$\bar{\tau} = \frac{|\Omega|}{(d^{-1} - 1)D} \left(\frac{1}{\varepsilon} + O(1) \right), \quad (16)$$

where $d < 1$ is the ratio of the radii [46]. Formula (16) indicates that a drastic reduction in flux can be achieved by putting an obstacle that limits the access to the absorbing window by forming a cusp-like passage (figure 10).

- (iv) For type (IV), when $\partial\Omega_a$ (of length a) is located at the end of a narrow neck with radius of curvature R_c (figure 8), the MFPT is given in [51, 52] as

$$\bar{\tau} = \frac{|\Omega|}{4D\sqrt{2a/R_c}} (1 + O(1)) \quad \text{for } a \ll |\partial\Omega|. \quad (17)$$

The MFPT to the narrow straits formed by a partial block of a planar domain (figure 10) is given by

$$\bar{\tau} = \sqrt{\frac{R_c(R_c + r_c)}{2r_c\varepsilon}} \frac{\pi |\Omega|}{2D} (1 + o(1)) \quad \text{for } \varepsilon \ll |\partial\Omega|, R_c, r_c, \quad (18)$$

where R_c and r_c are the curvatures at the neck and ε is the width of the straits. For a surface of revolution generated by rotating the curve in figure 8 about its axis of symmetry, we use the representation of the generating curve

$$y = r(x), \quad \Lambda < x < 0,$$

where the x -axis is horizontal with $x = \Lambda$ at the absorbing end AB . We assume that the parts of the curve that generate the funnel have the form

$$\begin{aligned} r(x) &= O(\sqrt{|x|}) \quad \text{near } x = 0 \\ r(x) &= a + \frac{(x - \Lambda)^{1+\nu}}{\nu(1+\nu)\ell^\nu} (1 + o(1)) \\ &\quad \text{for } \nu > 0 \quad \text{near } x = \Lambda, \end{aligned} \quad (19)$$

where $a = \frac{1}{2}\overline{AB} = \varepsilon/2$ is the radius of the gap, and the constant ℓ has dimension of length. For $\nu = 1$ the parameter ℓ is the radius of curvature R_c at $x = \Lambda$. The MFPT from the head to the absorbing end AB is given by

$$\bar{\tau} \sim \frac{\mathcal{S}(\Lambda)}{2D} \frac{\left(\frac{\ell}{(1+\nu)a}\right)^{\nu/1+\nu} \nu^{1/1+\nu}}{\sin \frac{\nu\pi}{1+\nu}}, \quad (20)$$

where \mathcal{S} is the entire unscaled area of the surface. In particular, for $\nu = 1$ the MFPT (20) reduces to

$$\bar{\tau} \sim \frac{\mathcal{S}}{4D\sqrt{a/2\ell}} \quad (21)$$

(compare with (14)). The case $\nu = 0$ corresponds to a conical funnel with an absorbing circle of small radius a (see figure 11) [51, 55]. For a sphere (21) reduces to (14) (figure 5 (right)). Formulae (17)–(21) indicate that efficient control of the flux can be achieved by putting the absorbing window at the end of a narrow symmetric or asymmetric funnel (figures 8–10). This type of funnel can be formed by crowding obstacles on the membrane surface (figure 17(a)), which results in an effective coarse-grained diffusion coefficient on the surface, different from the microscopic diffusion coefficient (see section 5.3).

- (v) In domains of type (V) a bulky head is connected to an essentially one-dimensional strip (or cylinder) of small radius a and length L , as is the case of a neuronal spine membrane. The connection of the head to the neck can be at an angle or by a smooth funnel (figures 4 and 9 (left), the narrow cylindrical neck is Ω_2). The boundary of the domain reflects Brownian trajectories and only the end of the cylinder $\partial\Omega_a$ absorbs them. In the three-dimensional case the Dirichlet boundary $\partial\Omega_a$ is a small absorbing disk at the end of the cylinder. The domain Ω_1 is the one shown in figure 8 and it is connected to the cylinder at an interface $\partial\Omega_i$, which in this case is the interval AB in figure 8. It was shown in [55] that the MFPT from $x \in \Omega_1$ to $\partial\Omega_a$ is given by

$$\bar{\tau}_{x \rightarrow \partial\Omega_a} = \bar{\tau}_{x \rightarrow \partial\Omega_i} + \frac{L^2}{2D} + \frac{|\Omega_1|L}{|\partial\Omega_a|D}. \quad (22)$$

Figure 13 shows that the smoothness of the neck connection makes a big difference in the MFPT. Formula (22) explains the role of a narrow neck in flux regulation. The flux dependence on the neck length is quite strong.

- (vi) A dumbbell-shaped domain (of type (VI)) consists of two compartments Ω_1 and Ω_3 and a connecting neck Ω_2 that is effectively one-dimensional, such as shown in figure 9 (right), or in a similar domain with a long neck. A Brownian trajectory that hits the segment AB at the center of the neck Ω_2 is equally likely to reach either compartment before the other; thus AB is the SS. Therefore, the mean time to traverse the neck from compartment Ω_1 to compartment Ω_3 is asymptotically twice the MFPT $\bar{\tau}_{\Omega_1 \rightarrow SS}$. Neglecting, as we may, the mean residence time of a Brownian trajectory in Ω_2 relative to

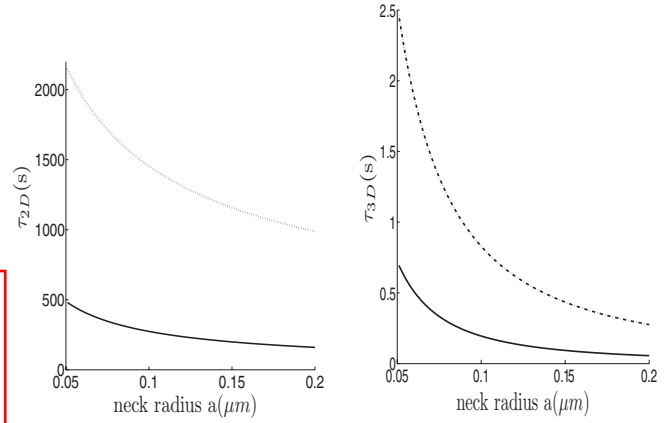


Figure 13. Left: the NET of Brownian motion on the surface of revolution obtained by revolving figure 4 (left) about its axis of symmetry (dashed line) and by revolving figure 4 (right) (solid line). Right: the NET in the corresponding solids of revolution. The smoothness of the connection makes a big difference.

that in Ω_1 or in Ω_3 we can write the transition rates from Ω_1 to the Ω_3 and vv as

$$\lambda_{\Omega_1 \rightarrow \Omega_3} = \frac{1}{2\bar{\tau}_{\Omega_1 \rightarrow SS}}, \quad \lambda_{\Omega_3 \rightarrow \Omega_1} = \frac{1}{2\bar{\tau}_{\Omega_3 \rightarrow SS}}. \quad (23)$$

These rates can be found from the explicit expression (1) for the flux into an absorbing window

$$\lambda_1 \sim \frac{1}{\bar{\tau}}, \quad (24)$$

where $\bar{\tau}$ is given in (22). Here $\bar{\tau}_{x \rightarrow \partial\Omega_i}$ is any one of the MFPTs given above, depending on the geometry of Ω_1 with L half the length of the neck and with $SS = \partial\Omega_a$. The radii of curvature $R_{c,1}$ and $R_{c,3}$ at the two funnels may be different in Ω_1 and Ω_3 . The smallest positive eigenvalue λ of the Neumann problem for the Laplace equation in the dumbbell is to leading order $\lambda = -(\lambda_{\Omega_1 \rightarrow \Omega_3} + \lambda_{\Omega_3 \rightarrow \Omega_1})$. For example, if the solid dumbbell consists of two general heads connected smoothly to the neck by funnels (see (29)), the two rates are given by

$$\begin{aligned} \frac{1}{\lambda_{\Omega_1 \rightarrow \Omega_3}} &= \sqrt{2} \left[\left(\frac{R_{c,1}}{a} \right)^{3/2} \frac{|\Omega_1|}{R_{c,1}D} \right] (1 + o(1)) \\ &\quad + \frac{L^2}{4D} + \frac{|\Omega_1|L}{\pi a^2 D} \\ \frac{1}{\lambda_{\Omega_3 \rightarrow \Omega_1}} &= \sqrt{2} \left[\left(\frac{R_{c,3}}{a} \right)^{3/2} \frac{|\Omega_3|}{R_{c,3}D} \right] (1 + o(1)) \\ &\quad + \frac{L^2}{4D} + \frac{|\Omega_3|L}{\pi a^2 D} \end{aligned} \quad (25)$$

(see [51]). Formulae (25) indicate that the unidirectional fluxes between the two compartments of a dumbbell-shaped domain can be controlled by the area (or surface area) of the two and by the type of obstacles to the access to the connecting neck. The equilibration rate in the dumbbell, λ , is thus controlled by the geometry.

- (vii) The mean time to escape through N well-separated absorbing windows of lengths a_j at the ends of funnels

with radii of curvature ℓ_j , respectively, in the boundary $\partial\Omega$ of a planar domain Ω is given by

$$\bar{\tau} = \frac{\pi |\Omega|}{2D \sum_{j=1}^N \sqrt{a_j/\ell_j}} (1 + o(1)) \quad \text{for } a_j/\ell_j \ll |\partial\Omega|. \quad (26)$$

The probability to escape through window i is given by

$$p_i = \frac{\sqrt{a_i/\ell_i}}{\sum_{j=1}^N \sqrt{a_j/\ell_j}}. \quad (27)$$

Formulae (26) and (27) are significant for diffusion in a network of compartments connected by narrow passages (e.g. on a membrane strewn with obstacles). The dependence of the MFPT $\bar{\tau}$ and of the transition probabilities p_i on the local geometrical properties of the compartments renders the effective diffusion tensor in the network position-dependent and can give rise to anisotropic diffusion.

- (viii) If the domain contains a deep potential trap the Brownian trajectory can be in any one of the following three states: trapped in the well, diffusing in the domain outside the well, and be absorbed in the small absorbing window. The MFPT to the window was calculated in [56].

4.2. Formulae for $\bar{\tau}$ in three-dimensional domains

The interpretation of the formulae for the cases (1)–(6) is much the same as for the two-dimensional case.

- (i) The MFPT to a circular absorbing window $\partial\Omega_a$ of small radius a centered at $\mathbf{0}$ on the boundary $\partial\Omega$ is given by [57]

$$\bar{\tau}_{x \rightarrow \partial\Omega_a} = \frac{|\Omega|}{4aD \left[1 + \frac{L(\mathbf{0}) + N(\mathbf{0})}{2\pi} a \log a + o(a \log a) \right]}, \quad (28)$$

where $L(\mathbf{0})$ and $N(\mathbf{0})$ are the principal curvatures of the boundary at the center of $\partial\Omega_a$.

- (ii) The MFPT from the head of the solid of revolution, obtained by rotating the symmetric domain in figure 8(left) about its axis of symmetry, to a small absorbing window $\partial\Omega_a$ at the end of a funnel is given by

$$\bar{\tau} = \frac{1}{\sqrt{2}} \left(\frac{R_c}{a} \right)^{3/2} \frac{|\Omega|}{R_c D} (1 + o(1)) \quad \text{for } a \ll R_c, \quad (29)$$

where the R_c is the radius of curvature of the rotated curve at the end of the funnel [51].

- (iii) The MFPT from a point x in a bulky head Ω to an absorbing disk $\partial\Omega_a$ of a small radius a at the end of a narrow neck of length L , connected to the head at an interface $\partial\Omega_i$, is given by the connection formula (22). When the cylindrical neck is attached to the head at a right angle the interface $\partial\Omega_i$ is a circular disk and $\bar{\tau}_{x \rightarrow \partial\Omega_i}$ is given by (28). When the neck is attached smoothly through a funnel $\bar{\tau}_{x \rightarrow \partial\Omega_i}$ is given by (29).

- (iv) The mean time to escape through N well-separated absorbing circular windows or radii a_j at the ends of funnels with curvatures ℓ_j , respectively, is given by

$$\bar{\tau} = \frac{1}{\sqrt{2}} \frac{|\Omega|}{D \sum_{j=1}^N \ell_j \left(\frac{a_j}{\ell_j} \right)^{3/2}}. \quad (30)$$

The exit probability through window i is given by

$$p_i = \frac{a_i^{3/2} \ell_i^{-1/2}}{\sum_{j=1}^N a_j^{3/2} \ell_j^{-1/2}}. \quad (31)$$

- (v) The principal eigenvalue of the Laplace equation in a dumbbell-shaped structure is given in item (vi), equations (23)–(25) [51].
 (vi) The leakage flux through a circular hole of small radius a centered at $\mathbf{0}$ in the reflecting boundary is given by [57]

$$J_a = 4aDu_0(\mathbf{0}) + O\left(\frac{a^2}{|\Omega|^{2/3}} \log \frac{a}{|\Omega|^{1/3}}\right), \quad (32)$$

where $u_0(\mathbf{0})$ is the concentration of diffusers at the window in the same model without the absorbing window.

5. Applications to cellular biology and simulations

Some applications of the analytical approximations to the MFPT are listed below. The formulae quantify the structures and predict their functions. They are also used to verify the validity of large Brownian simulations, such as the ones used for predicting the synaptic current.

5.1. Applications to Brownian dynamics simulations

Brownian dynamics simulations of rare events are difficult and inefficient. Thus predicting from a simulation the diffusion current through narrow passages is often impossible, due to the small sample of passages of individual simulated Brownian trajectories through the opening. In this situation the analytical approximation gives reliable information where simulations fail. For example, the bottleneck in simulations of ionic permeation in protein channels is the arrival of ions from the salt solution to the channel. The arrival rate at a given small neighborhood of the channel can be calculated analytically and used in the simulation of the permeation process.

A similar situation arises in the simulation of the entire synaptic transmission, which contains the simulation of the arrival of neurotransmitter molecules at receptors on the post-synaptic membrane [29]. A significant reduction in the simulation complexity is achieved using the analytically computed neurotransmitter flux rather than simulating it [58]. Analytical formulae were also used for quantifying diffusion in dendritic spines [20]. Another increasing step was achieved for modeling chemical reactions by replacing complex Brownian simulations by Markov chains [58, 59]. In fact, using that the arrival of a stochastic particle to a small target is Poissonian [50], it is possible to approximate binding and unbinding in microdomains by a Markov chain

[58], opening the route for a complete analysis of stochastic chemical reactions, which is impossible by simulating complex reaction–diffusion involving partial differential equations, that in general cannot be solved. A recent application of this Markovian approximation concerns some novel prediction about the rate of molecular dynamics, underlying the spindle assembly check point during cell division [60].

Another application of asymptotic analytical results is the verification of molecular dynamics simulations in domains that contain small passages or targets [20]. The convergence of the simulation can be measured by the convergence of the statistics of rare events to that predicted by the analytical asymptotic approximation.

5.2. Synaptic transmission and the synaptic cleft

The neuronal cleft conducts neurotransmitters by diffusion from a vesicle released at the excitatory pre-synaptic membrane to receptors such as NMDA and AMPA located in the post-synaptic membrane (figures 2 (right) and 3). Synaptic transmission depends on various parameters such as the location of a released vesicle, the number and type of receptors, trafficking between the PSD and extra-synaptic compartments, as well as the synapse organization. It is now possible to quantify separately each of them using Brownian simulation and mixed analytical approaches [61, 62]. They might lead to a better understanding of pathological synapses, implicated in many cognitive disorders such as spectral autism disorders, epilepsy and many others [63, 64].

In the mathematical description of neurotransmitter diffusion in the synaptic cleft, the cleft geometry is simplified to a circular cylinder of length L and radius R , whose bases S_0 and S_L are centered at the z -axis, at $z = 0$ and $z = L$, respectively, and are parallel to the (x, y) plane. The lateral surface S_r , which is surrounded by glia cells (figures 3 (labeled G) and 12 (left)), absorbs the neurotransmitters that are injected at S_0 with a constant flux density ϕ . A receptor is represented as a small absorbing circular hole $S(a)$ of radius a on S_L . Both S_0 and S_L reflect the Brownian trajectories of the neurotransmitters. The small hole $S(a)$ (receptor) can be moved away from the center, thus controlling the flux through the hole with distance to the center. For a point source at $(z, r, \theta) = (0, 0, 0)$ (in cylindrical coordinates), the density at the other end $z = L$ is found in a straightforward manner to be

$$u_0(r, L, 0) = \sum_{m=1}^{\infty} \frac{L J_0\left(\frac{\gamma_{0,m} r}{R}\right)}{D \pi R \gamma_{0,m} J_0'^2(\gamma_{0,m}) \sinh \frac{\gamma_{0,m} L}{R}}, \quad (33)$$

where $\gamma_{n,m}$ are the roots of the Bessel function $J_n(\cdot)$. The probability that a Brownian particle injected at the source will reach a receptor centered at $(r, L, 0)$ is the probability that the time τ_{hole} to reach the absorbing window is shorter than the time τ_{S_r} to reach the lateral absorbing boundary (glia cells), given by

$$\Pr\{\tau_{\text{hole}} < \tau_{S_r}\} = \frac{4a}{\pi R} \sum_{m=1}^{\infty} \frac{J_0\left(\frac{\gamma_{0,m} r}{R}\right)}{\gamma_{0,m} J_0'^2(\gamma_{0,m}) \sinh \frac{\gamma_{0,m} L}{R}} + O\left(\frac{a^2}{L^2} \log \frac{a}{L}\right). \quad (34)$$

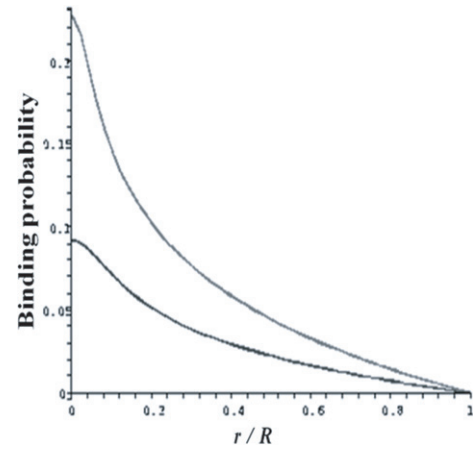


Figure 14. The probability that a neurotransmitter molecule injected to the cleft at $(0, 0, 0)$ will reach an AMPA receptor at $(r, L, 0)$ is the probability that the time τ_{hole} to reach the absorbing window is shorter than the time τ_{S_r} to reach the lateral absorbing boundary (glia cells), according to (34) (figure 3). $\varepsilon = 1\text{nm}$, 1 AMPAR in the PSD.

For $r = 0$ this reduces to

$$\Pr\{\tau_{\text{hole}} < \tau_{S_r}\} = \frac{4a}{\pi R} \sum_{m=1}^{\infty} \frac{1}{\gamma_{0,m} J_0'^2(\gamma_{0,m}) \sinh \frac{\gamma_{0,m} L}{R}} + O\left(\frac{a^2}{L^2} \log \frac{a}{L}\right). \quad (35)$$

The graph of (34) in figure 14 shows that a slight misalignment of the synaptic release or terminals may lead to a significant change in the number of neurotransmitters bound to receptors in the process of synaptic transmission. This suggests that a misalignment of the vesicular release with the receptor clustering can drastically reduce the number of open channels. This, in turn, can explain the key role of adhesion molecules, such as the Ephrin B, which regulate the localization of AMPA receptors [65]. Moreover, overexpression or knockdown of scaffolding molecules, such as PSD-95 in the post-synaptic cell, modulates pre-synaptic release probability, thus confirming the tight control of the release site compared with the accumulation of post-synaptic receptors [66]. This analysis of the physical model of the synaptic cleft reveals that changing the relative position of pre- and post-synaptic elements can drastically affect the open probability of receptors. The mathematical analysis of the physical model sheds some light on the complex electrophysiological data. Including additional synaptic components in the model may further clarify the specific role of adhesion molecules in controlling synaptic transmission. This includes glial transmitters or ATP. Another application of the MFPT formula is its application to the homogenization of boundary conditions for problems with many binding sites on the boundary. The homogenized boundary conditions simplify complex molecular (Brownian dynamics) simulations that include neurotransmitter release, binding to receptors, and flux through the opened channel [61, 62].

5.3. Diffusion on a membrane crowded with obstacles

The organization of a cellular membrane is to a large extent the determinant of the efficiency of molecular (e.g.

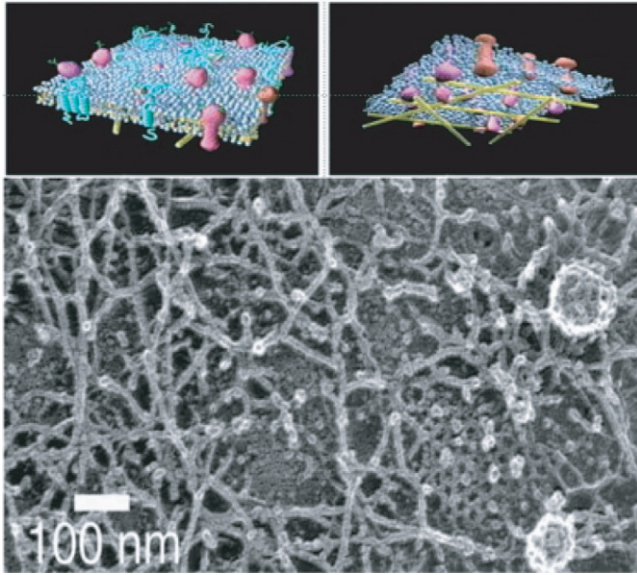


Figure 15. Organization of a neuronal membrane [68] containing microdomains made of overlapping filaments (see schematic figure 17(a)).

receptors) trafficking to their destination. The arrival rates of these molecules at their specific destinations control their role and performance, and thus steer the cell to achieve its function. After two decades of intense research on membrane organization [67–71, 73, 74] it is still unclear how the heterogeneity of the membrane controls diffusion (figure 15). Recently, using single molecule tracking, the diffusion coefficient of a molecule freely diffusing on intact and treated neuronal membranes, cleared of almost all obstacles, was reported in [75]. In this case the diffusion of a protein on the membrane is described by the classical Saffman–Delbrück theory [76]. If, however, the membrane is crowded with obstacles, such as fixed proteins, fences and pickets, and so on, the effective diffusion coefficient differs significantly from that predicted in [76] and depends strongly on the degree of crowding (see [72]). The latter can be estimated from diffusion data and from an appropriate model and its analysis, as explained below [52]. The key to assessing the crowding is to estimate the local diffusion coefficient from the measured molecular trajectories and the analytic formula for the MFPT through a narrow passage between obstacles (figure 16).

Specifically, a simplified model of a crowded membrane can be a square lattice of circular obstacles of radius a centered at the corners of lattice squares of side L (figure 17(a)). The mean exit time from a lattice box, formula (30), is to leading order independent of the starting position (x, y) and can be approximated by (26) as

$$\bar{\tau}_4 = \frac{\bar{\tau}}{4}, \quad (36)$$

where $\bar{\tau}$ is the MFPT to a single absorbing window in a narrow strait with the other windows closed (reflecting instead of absorbing). It follows that the waiting time in the cell enclosed by the obstacles is exponentially distributed (1) with rate

$$\lambda = \frac{2}{\bar{\tau}_4}, \quad (37)$$

where $\bar{\tau}$ is given by (15) and (18) as

$$\bar{\tau} \approx \begin{cases} c_1 & \text{for } 0.8 < \varepsilon < 1, \\ c_2 |\Omega| \log \frac{1}{\varepsilon} + d_1 & \text{for } 0.55 < \varepsilon < 0.8, \\ c_3 \frac{|\Omega|}{\sqrt{\varepsilon}} + d_2 & \text{for } \varepsilon < 0.55, \end{cases} \quad (38)$$

with $\varepsilon = (L - 2a)/a$ and $d_1, d_2 = O(1)$ for $\varepsilon \ll 1$ (figure 18). The constants c_i , ($i = 1, 2, 3$) are calculated in [52]: $c_1 \approx [4L^2/\pi^3 D][\cosh(\pi/2 - 1)/\cosh \pi]$ remains unchanged and with $L = 1, D = 1$, we find $c_1 \approx 0.076$. Similarly, $c_2 = 1/2\pi D \approx 0.16$. However, the coefficient c_3 is obtained by $c_3 \approx \pi/8 D \approx 0.39$.

The coefficients d_i are chosen by patching $\bar{\tau}$ continuously between the different regimes. We obtain

$$d_1 = c_1 + c_2 |\Omega(r_1)| \log(1 - 2r_1), \quad (39)$$

and

$$d_2 = c_1 - c_2 [|\Omega(r_1)| \log(1 - 2r_1) + |\Omega(r_2)| \log(1 - 2r_2)] - c_3 |\Omega(r_2)| r_2^{1/2} (1 - 2r_2)^{-1/2}, \quad (40)$$

where $|\Omega(r)| = L^2 - \pi r^2$. Equation (38) holds in the full range of values of $a \in [0, L/2]$ and L .

The Brownian motion between the obstacles (figure 17(a)) can be coarse-grained into a Markovian random walk that jumps between the connected domains at exponentially distributed times with rates determined by the MFPTs and exit probabilities. This random walk can in turn be approximated by an effective coarse-grained anisotropic diffusion, as carried out for atomic migration in crystals [77, chapter 8, section 2] and for effective diffusion on a surface with obstacles [52]. The diffusion approximation to the transition probability density function of an isotropic random walk that jumps at exponentially distributed waiting times with rate λ on a square lattice with step size L is given by [77]

$$\frac{\partial p}{\partial t} = \bar{D} \left(\frac{\partial^2 p}{\partial x^2} + \frac{\partial^2 p}{\partial y^2} \right), \quad \bar{D} = \frac{\lambda L^2}{4}. \quad (41)$$

To illustrate this theory, we assume a reduction in the effective diffusion coefficient from 0.01 on a clear membrane to $0.2 \mu\text{m}^2 \text{s}^{-1}$ on an obstructed membrane [78], which leads to the estimate of 70% occupancy of the membrane surface with obstacles [52], as can be seen from figures 17(b)–(d).

5.4. Stochastic chemical reactions in microdomains

Traditional chemical kinetics, based on mass action laws or reaction–diffusion equations, give an inappropriate description of the stochastic chemical reactions in microdomains, where only a small number of substrate and reactant molecules are involved. A Markovian description of the stochastic dynamics of the binding and unbinding of molecules is given in [53] and applied in [59, 60].

Consider two finite species, the mobile reactant M that diffuses in a bounded domain Ω and the stationary substrate S (e.g. a protein) that binds M . The boundary $\partial\Omega$ of the domain Ω is partitioned into an absorbing part $\partial\Omega_a$ (e.g. pumps, exchangers, another substrate that forms permanent bonds with M , and so on) and a reflecting part $\partial\Omega_r$ (e.g. a cell

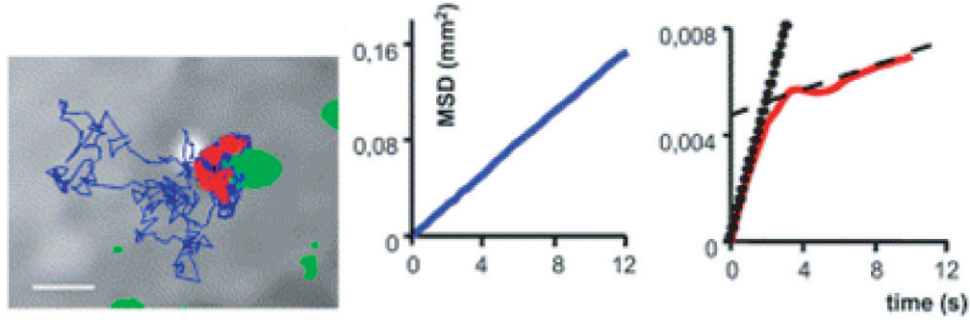


Figure 16. Left: trajectories of receptors moving on a neuronal membrane. Reproduced by permission from Macmillan Publishers Ltd [78], copyright 2003. The trajectory switches between confined (red) and free (blue) periods. The synaptic domain is marked green. Right: mean square displacement (MSD) versus time without confinement and with confinement.

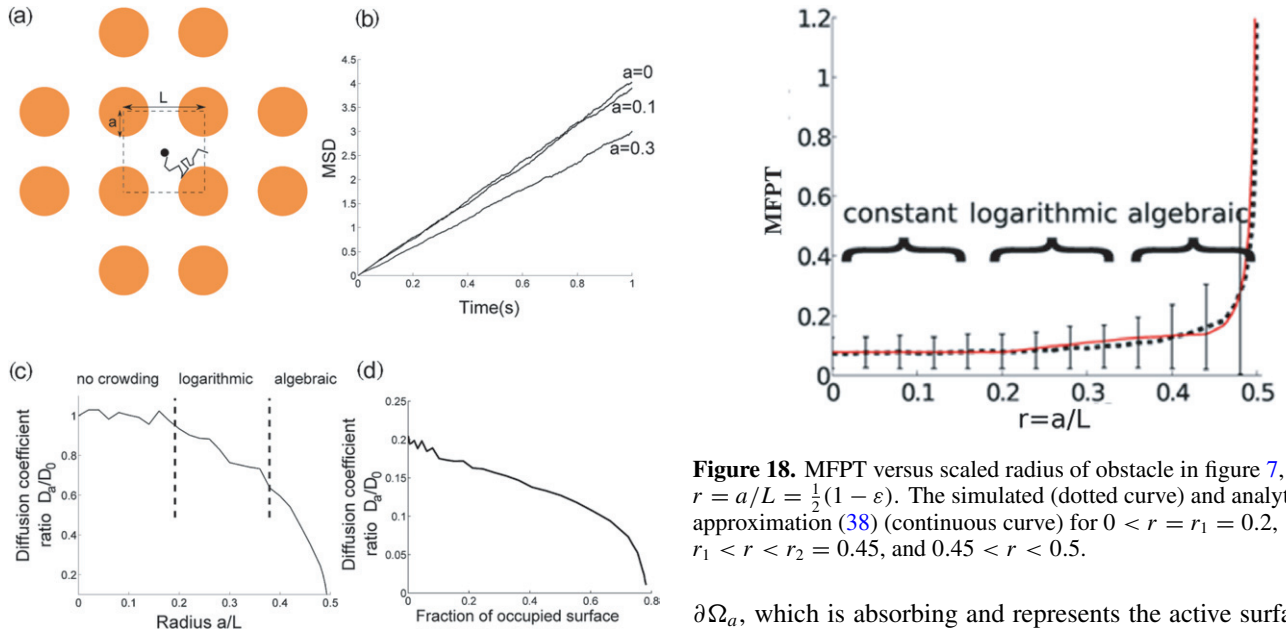
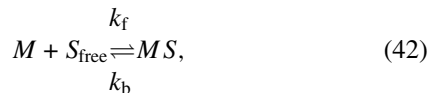


Figure 17. (a) Schematic representation of a Brownian particle diffusing in a crowded microdomain. (b) Effective diffusion coefficient $\bar{D} = L^2/2\bar{\tau}$ as a function of time. (c) \bar{D} for different radii of the obstacles. The three regions of $\bar{\tau}$ are separated by dashed lines. The solid curve represents Brownian simulations. While there is no crowding for $a < 0.2$, the decreasing of the effective diffusion coefficient for $0.2 < a < 0.4$ is logarithmic, and like square root for $a > 0.4$. (d) Effective diffusion coefficient vs fraction of occupied surface.

membrane). In this model the volume of M is neglected. In terms of traditional chemical kinetics the binding of M to S follows the law



where k_f is the forward binding rate constant, k_b is the backward binding rate constant, and S_{free} is the unbound substrate. We assume in our model of the reaction that the M molecules diffuse in Ω independently and when bound, are released independently of each other at exponential waiting times with rate k_{-1} .

For a single molecule, the time to binding is the first passage time to diffuse to a small portion of the boundary,

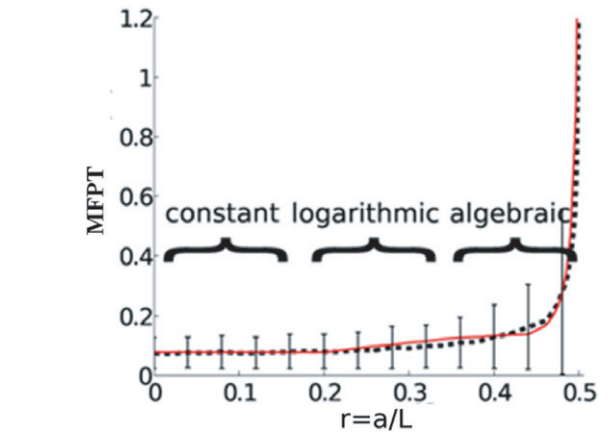


Figure 18. MFPT versus scaled radius of obstacle in figure 7, $r = a/L = \frac{1}{2}(1 - \varepsilon)$. The simulated (dotted curve) and analytical approximation (38) (continuous curve) for $0 < r = r_1 = 0.2$, $r_1 < r < r_2 = 0.45$, and $0.45 < r < 0.5$.

$\partial\Omega_a$, which is absorbing and represents the active surface of the receptor, whereas the remaining part of $\partial\Omega$ is reflecting. Due to the small target and to the deep binding potential well the binding and unbinding of M to S are rare events on the time scale of diffusion [50]. This implies that the probability distribution of binding times is approximately exponential [37] with rate $\lambda_1 = 1/\langle\tau_1\rangle$, where $\langle\tau_1\rangle$ is the MFPT to $\partial\Omega_a$. When there are S binding sites, $k(t)$ of which are unbound, there are $N = [M - S + k]^+$ free diffusing molecules in Ω , where $x^+ = \max\{0, x\}$. The arrival time of a molecule to the next unbound site is well approximated by an exponential law with state-dependent instantaneous rate (see discussion in [53])

$$\lambda_k = \frac{Nk}{\langle\tau_1\rangle} = \frac{k(M - S + k)^+}{\langle\tau_1\rangle}.$$

The number $k(t)$ of unbound receptors at time t is a Markovian birth-death process with states $0, 1, 2, \dots, \min\{M, S\}$ and transition rates $\lambda_{k \rightarrow k+1} = \lambda_k$, $\lambda_{k \rightarrow k-1} = \mu = k_{-1}$. The boundary conditions are $\lambda_{S \rightarrow S+1} = 0$ and $\lambda_{0 \rightarrow -1} = 0$. Setting $P_k(t) = \Pr\{k(t) = k\}$ we write the Kolmogorov equations for the transition probabilities [53]

$$\begin{aligned} \dot{P}_k(t) = & -[\lambda_k + k_{-1}(S - k)]P_k(t) + \lambda_{k+1}P_{k+1}(t) \\ & + k_{-1}(S - k + 1)P_{k-1}(t) \\ & \text{for } k = (S - M)^+ + 1, \dots, S - 1 \end{aligned} \quad (43)$$

with the boundary equations

$$\begin{aligned}\dot{P}_{(S-M)^+}(t) &= -k_{-1}SP_{(S-M)^+}(t) + \lambda_1 P_{(S-M)^++1}(t) \\ \dot{P}_S(t) &= -\lambda_S P_S(t) + k_{-1}P_{S-1}(t).\end{aligned}$$

The initial condition is $P_{k,q}(0) = \delta_{k,S}\delta_{q,0}$. Our purpose is to calculate the average number unbound (or bound) sites $\langle k(t) \rangle$, which for $t \rightarrow \infty$ is given by $\langle k_\infty \rangle = \sum_{j=(S-M)^+}^S j P_j$, where $P_j = \lim_{t \rightarrow \infty} P_j(t)$. Similarly, the stationary variance in the number unbound sites is $\sigma^2(M, S) = \langle k_\infty^2 \rangle - \langle k_\infty \rangle^2$, where $\langle k_\infty^2 \rangle = \sum_{j=(S-M)^+}^S j^2 P_j$. The results of the Markovian model are

$$\begin{aligned}P_S &= \frac{1}{1 + \sum_{k=1}^{S-(S-M)^+} \frac{\prod_{i=S-k+1}^S i(M-S+i)^+}{k!((\tau_1)k_{-1})^k}} \\ \langle k_\infty \rangle &= P_S \sum_{k=S-1}^{(S-M)^+} (S-k)^+ \frac{\prod_{i=S-k+1}^S i(M-S+i)^+}{k!((\tau_1)k_{-1})^k} \\ \langle k_\infty^2 \rangle &= P_S \sum_{k=S-1}^{(S-M)^+} [(S-k)^+]^2 \frac{\prod_{i=S-k+1}^S i(M-S+i)^+}{k!((\tau_1)k_{-1})^k} \\ \sigma_S^2(M) &= \langle k_\infty^2 \rangle - \langle k_\infty \rangle^2\end{aligned}\quad (44)$$

(see [53] for further details).

These formulae were used in [53] to estimate the fraction of bound receptors in photo-receptor outer segments and also to interpret the channel noise measurements variance. This analysis was used in [29] to estimate the number of bound AMPA receptors in the post-synaptic density. A similar gated Markovian model was proposed in [54].

Another application of the Markovian model is the calculation of the mean time the number of bound molecules reach a threshold (MTT). In a cellular context, the MTT can be used to characterize the stability of chemical processes, especially when they underlie a biological function. Using the previous Markov-chain description, we estimate the MTT in terms of fundamental parameters, such as the number of molecules, the ligands and the forward and backward binding rates. Interestingly, as we shall see the MTT depends non-linearly on the threshold T .

We consider M Brownian molecules inside a microdomain that can bind to immobile targets S , modeled generically by equation (42). The (random) first time the (random) number $[MS](t)$ of MS molecules at time t reaches the threshold is defined as

$$\tau_T = \inf\{t > 0 : [MS](t) = T\} \quad (45)$$

and its expected value is $\bar{\tau}_T$. We consider $\bar{\tau}_T$ for an ensemble of the targets initially free and distributed on the surface of a closed microdomain for vanishing backward rate ($k_{-1} = 0$) and for $k_{-1} > 0$. The dynamical system for the transition probabilities of the Markov process $MS(t)$ is similar to that in the previous section, but for the absorbing boundary condition at the threshold T , which gives 43 [59]. When the binding is irreversible ($k_{-1} = 0$), $\bar{\tau}_T$ is the sum of the forward rates

$$\tau_T^{\text{irrev}} = \frac{1}{\lambda_0} + \frac{1}{\lambda_1} + \dots + \frac{1}{\lambda_{T-1}} = \frac{1}{\lambda} \sum_{k=0}^{T-1} \frac{1}{(M_0 - k)(S_0 - k)}. \quad (46)$$

In particular, when $M_0 = S_0$ and $M_0 \gg 1$ (46) becomes asymptotically $\tau_T^{\text{irrev}} \approx T/\lambda M_0(M_0 - T)$. In addition, when the diffusing molecules largely exceed the number of targets ($M_0 \gg S_0, T$), (46) gives the asymptotic formulae

$$\tau_T^{\text{irrev}} \approx \begin{cases} \frac{1}{\lambda M_0} \log \frac{S_0}{S_0 - T} & \text{for } M_0 \gg S_0, T \\ \frac{1}{\lambda S_0} \log \frac{M_0}{M_0 - T} & \text{for } S_0 \gg M_0, T \\ \frac{T}{\lambda M_0 S_0} & \text{for } M_0, S_0 \gg T. \end{cases} \quad (47)$$

Figure 19 shows the plot of τ_T^{irrev} for several values of the threshold T , compared with Brownian simulations in a circular disk $\Omega = D(R)$ with reflecting boundary, except at the targets.

When $k_{-1} > 0$ the asymptotic formulae are given by [59]

$$\bar{\tau}_T \approx \begin{cases} \tau_T^{\text{irrev}} + \frac{k_{-1}}{(\lambda M_0)^2} \left[\frac{T}{S_0 - T} - \log \left(1 + \frac{T}{S_0 - T} \right) \right] & \text{for } M_0 \gg S_0, T \\ \tau_T^{\text{irrev}} + \frac{k_{-1}}{(\lambda S_0)^2} \left[\frac{T}{M_0 - T} - \log \left(1 + \frac{T}{M_0 - T} \right) \right] & \text{for } S_0 \gg M_0, T \\ \tau_T^{\text{irrev}} + \frac{k_{-1}}{2\lambda^2} \left(\frac{T}{M_0^2} \right)^3 & \text{for } S_0 = M_0 \gg T. \end{cases}$$

Thus τ_T varies quadratically with the MFPT $\bar{\tau} = 1/\lambda$, and is a nonlinear increasing function of T . These computations are quite general and can be applied to describe the mean time to reach a threshold for any chemical reaction. Changing the threshold modulates the threshold time in an efficient way [59, 60].

5.5. Regulation of calcium flux through the dendritic spine neck

Although the function of dendritic spines is still unclear, one of their identified role is to dynamically filter calcium ions [15–17]. One mechanism to filter ions would be to extrude them from exchangers located on the spine apparatus in the neck.

In the mathematical description of the diffusion of calcium ions from the spine head to the dendrite, the spine neck is a circular cylinder of length L and radius R , whose bases S_0 and S_L are centered at the z -axis, at $z = 0$ and $z = L$, respectively, and are parallel to the (x, y) plane. The lateral surface S_r , which in general represents the internal membrane of the endoplasmic reticulum, is reflecting. A constant net flux ϕ is injected at S_0 . A rapid exchanger is modeled as a small absorbing circular hole $S(a)$ of radius a on S_r , which may represent an ion pump (figure 12 (right)). The leakage formula (32) and the explicit expression $u(\mathbf{0}) = \phi(L - z)/\pi DR^2$, which replaces (33) in this case, give the flux through $S(a)$ as $J_a = 4a\phi(L - z)/\pi R^2$. It is thus possible to estimate the leak of any ion in the spine neck [18, 57].

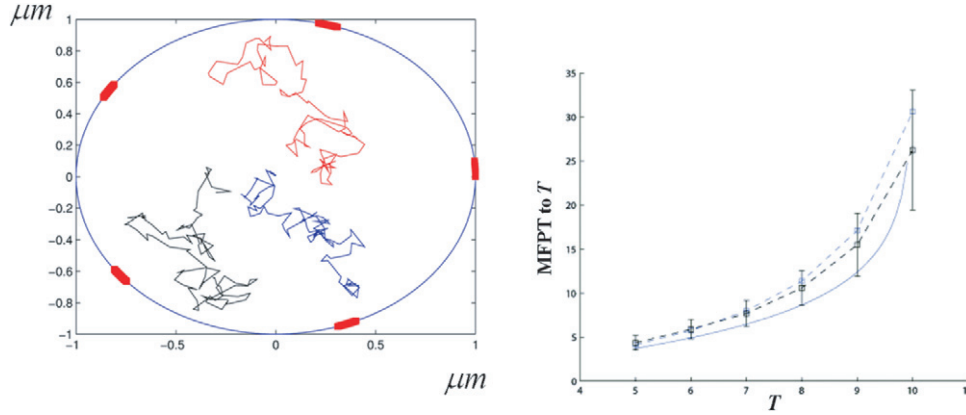


Figure 19. Left: trajectories of diffusing molecules in a circular disk containing five binding sites on the boundary. Right: MFPT τ_T^{irrev} to threshold T as a function of T in the irreversible case ($k_{-1} = 0$). Brownian simulations (blue dash), formula (46) (black dash), and its approximation (47) (continuous blue line). The other parameters are $S_0 = 15$, $M_0 = 10$, $\epsilon = 0.05$, $D = 0.1 \mu\text{m}^2 \text{s}^{-1}$ and the radius of the disk is $R = 1 \mu\text{m}$ (200 runs).

5.6. Delivery of vesicles in neurite outgrowth

Neurite outgrowth is a fundamental process of development, which requires both membrane expansion by exocytosis and cytoskeletal dynamics. To study the specific contribution of these processes and to account for live imaging data, a biophysical model was used in [88] to relate the overall neurite outgrowth rate to the rate of vesicle delivery at the growth cone tip. The vesicle motion was modeled as isotropic diffusion in a spherical domain of radius R with constant radial potential $U(x) = -v(x) \cdot x$, where $v(x)$ is the constant field of radial average motion away from the center. This model represents the motion of vesicles in the cell soma by a combination of Brownian motion and directed motion along microtubules and actin filaments. The MFPT to a small neurite initiation site of radius a on the surface was shown to be given in the large force limit by

$$\bar{\tau} = \frac{|S|}{a|v|} \left(1 + O\left(\frac{D}{|v|R}\right) \right). \quad (48)$$

where $|S|$ is the surface area of the soma. Formula (48) reveals that unlike (28) for Brownian motion, the search time in this case depends on the boundary surface due to the sequestration at the surface by the strong drift. Simulations show that the Brownian trajectories stay close to the boundary surface in their search for the absorbing window [88]. The derivation of (48) relies on the three-dimensional NET formula for Brownian motion in a potential field in the limit of high velocity $|v|$ [56].

This biophysical analysis revealed that in the absence of microtubules, a nascent neurite initiated by vesicular delivery can only reach a small length [88]. By adding the microtubule dynamics to the secretory pathway in stochastic analysis and simulations, it was possible to study the complex dynamics of neurite growth (figure 20): within this model, depending on the coupling parameter between the microtubules and the neurite, three different growing modes including the stable axonal growth and the stochastic dendritic growth, a fast oscillatory regime. To validate one aspect of the model, it was demonstrated that the experimental flux of TI-VAMP but not Synaptobrevin 2 vesicles contributes to the neurite growth.

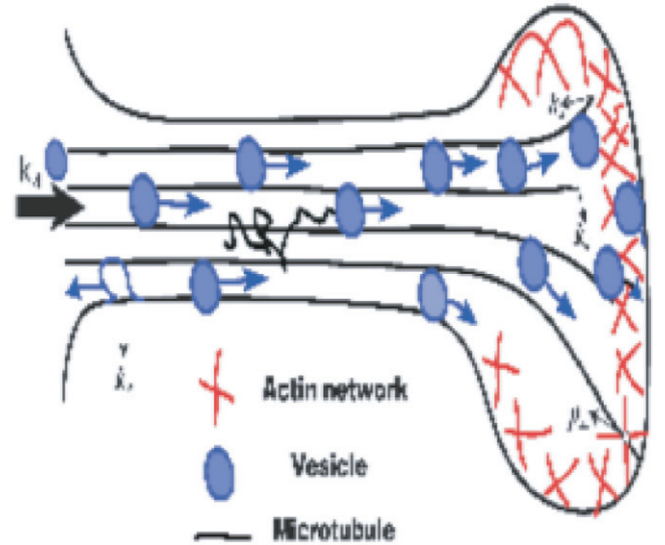


Figure 20. Vesicular delivery during neurite outgrowth. The vesicle switches between directed motion along microtubules and Brownian motion in the dendrite until it fuses with the membrane [88].

5.7. DNA repair in a two-dimensional confined chromatin structure

A Brownian needle in a strip can model a mRNA, a transcription factor, or a stiff DNA fragment moving in the very confined chromatin structure. For example, under severe stress, the DNA of the bacterium *Deinococcus radiodurans*, the most radioresistant organism, undergoes a phase transition in reorganizing the genome into tightly packed toroids (figures 21(a)–(c)), which may facilitate DNA repair [79]. Three-dimensional analysis [80] reveals a complex network of double membranes that engulf the condensed DNA, suggesting that two-dimensional domains lying between parallel walls may play a significant role in DNA repair.

The diffusion of the needle is characterized by three diffusion coefficients: longitudinal along the axis D_X , transversal D_Y and rotational D_r . The diffusive motion of a needle confined to a planar strip, which is only slightly wider

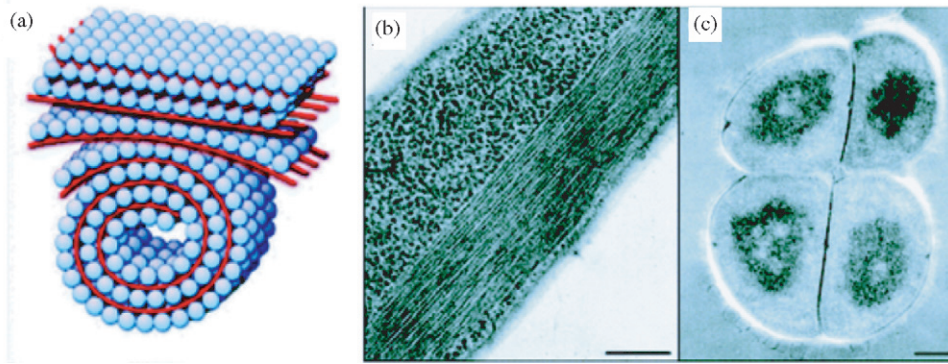


Figure 21. (a) Two-dimensional stratification: the model depicts the toroidal morphology that acts as a structural template for growth of the DNA–(DNA-binding protein) co-crystal. The DNA (red stripe) is localized in between the pseudo-hexagonal faces of the dodecameric symmetric proteins (blue spheres, reproduced with permission from [80]. Copyright 1991, Annual Reviews, Inc.) Figure 22 is a schematic model of the motion of a broken DNA strand in this geometry. (b) Two-dimensional arrangement of DNA: formation of DNA-RecA ‘repaosome’ assemblies in *E. coli* cells exposed to DNA-damaging agents. The ordered intracellular assembly is promoted by DNA molecular condensation and the structural features are modulated by the RecA proteins. Scale bar, 200 nm. (c) DNA packaging in the radioresistant bacteria *D. radiodurans*. The electron micrograph depicts the toroidal organization of its genome. Within this structure, the tight and ordered packaging of the DNA molecule may facilitate repair of double-stranded DNA breaks. Scale bar, 400 nm. The genomic reorganization in bacterial systems into tightly packed structures is proposed to restrict molecular diffusion.

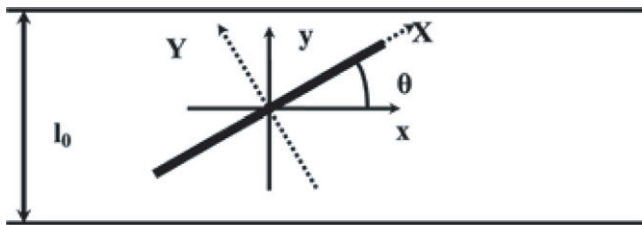


Figure 22. Rod in strip. The strip width is l_0 and the needle length is $l < l_0$. The position of the needle is characterized by the angle θ and the fixed coordinates x, y of the center or in a rotating system of coordinates (X, Y, θ) .

than the length of the needle, its turning around is a rare event (see figure 22). This is due to the narrow space around the vertical position of the needle in the strip. If the length of the needle l is only slightly smaller than the width of the strip $l_0 > l$, such that $\varepsilon = (l_0 - l)/l_0 \ll 1$, then mean time for the needle to turn 180° is given by [82]

$$\bar{\tau} = \frac{\pi \left(\frac{\pi}{2} - 1\right)}{D_r \sqrt{l_0(l_0 - l)}} \sqrt{\frac{D_x}{D_r}} \left(1 + O\left(\sqrt{\frac{l_0 - l}{l_0}}\right)\right). \quad (49)$$

Formula (49) shows that when the free space between two planes decreases, the effective diffusion constant, proportional to the reciprocal of $\bar{\tau}$, experiences a second order phase transition, characterized by a discontinuity of the derivative of the effective diffusion constant for the rotation (reciprocal of the MFPT (49)). Specifically, when the variable l reaches and exceeds the value $l = l_0$ the diffusion constant vanishes. This result explains the crucial role of the chromatin organization in maintaining the genome integrity during heavy radiation stress.

The phase transition indicated by (49) was reported experimentally several times [79–81]. It should be associated with the high probability of DNA repair by preventing the broken DNA strand to drift apart or become misaligned by turning over.

5.8. Hidden binding sites control chemical reactions

Active sites of a complex molecule, such as hemoglobin, penicillin-binding proteins, and many others, are often hidden inside the complex organization of α - and β -sheet structures. A ligand, such β -lactam antibiotic, has to bind to a small site hidden inside the molecule and indeed, ligand recognition requires that strands be antiparallel in the active site area. This phenomenon was observed for large antibiotic molecules. In figures 23(2) and (3) the penicillin-binding proteins are in closed and conformations, respectively [83]. In the closed conformation (figures 23 (2 and 3 right)) the active site is blocked and unavailable for binding, while in the open state (figures 23 (2 and 3 left)) the catalytic funnel reveals an elongated binding cleft, where the active site (red arrow) is hidden at the bottom. The activation time for this case can be estimated from the funnel shape using the asymptotic formula (20). When the site can switch between an active and inactive state, the effective rate constant can be estimated using the gated narrow escape theory of [84] (see also [85]).

5.9. Asymmetric dumbbell-shaped division in cell

An intermediate stage of a dividing cell consists of an asymmetric dumbbell shape with a relatively long connecting neck (figures 11 and 24). In this stage, some of the genetic material is delivered from the bigger (mother) to the smaller compartment (daughter). An open debate in this field is how the genetic material is selected? A recent report [86] proposes that diffusion through the connecting neck is the main determinant of the delivery rate and of the selection of fast diffusing particles during the transient regime, before steady state is reached. In fact, the present analysis confirms that in the absence of any active mechanism, the control of the delivery process can be realized by a drastic slowdown of the back flow from the daughter to the mother cell by an asymmetry in the curvature of connecting neck in the smaller

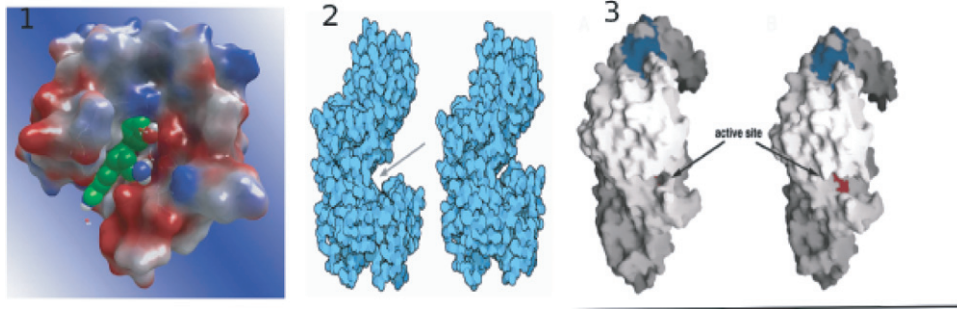


Figure 23. (1) Complex molecule containing a hidden site. The domain Ω is the surrounding fluid, the absorbing boundary $\partial\Omega_a$ is the hidden target (marked green), and the reflecting boundary $\partial\Omega_r$ is the remaining surface of the molecule. (2) Hidden site. (3) Hidden active site. Copyright (2005) National Academy of Sciences, USA.

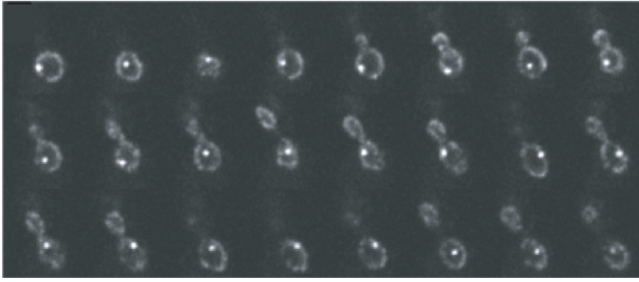


Figure 24. Time-lapse images of mitotic cells: the dumbbell-shaped dividing cell seems to vary with time. Reproduced from [86], Copyright 2011, with permission from Elsevier.

compartment, as described in the asymptotic formulae (23)–(25) for the mean residence times $\bar{\tau}$ in the compartments. Specifically, the mean time to go from mother to daughter is given by $\tau_{M \rightarrow D} \sim 2\bar{\tau}_{M \rightarrow SS}$ and in the other direction by $\tau_{D \rightarrow M} \sim 2\bar{\tau}_{D \rightarrow SS}$ in the limit of a narrow neck. The transition rates given in (23) can differ by orders of magnitude as the geometry changes. This can explain some of the findings reported experimentally in [86]. The rate of equilibration between the two compartments can be found from the estimate of the second eigenvalue μ of the Neumann problem in the dumbbell-shaped domain, given by

$$\frac{1}{\mu} = \frac{1}{\tau_{D \rightarrow M}} + \frac{1}{\tau_{M \rightarrow D}}.$$

When the time scale of morphological changes in the shape of the dumbbell is slower than diffusion, the protein and genetic material transferred by diffusion from the mother to the daughter cell can be estimated from a reduced system of equations for the mass in the mother and daughter cells, M_M and M_D , respectively, given by

$$\begin{aligned} \dot{M}_D &= -\frac{M_D}{\tau_{M \rightarrow D}} + \frac{M_M}{\tau_{D \rightarrow M}} \\ \dot{M}_M &= -\frac{M_M}{\tau_{D \rightarrow M}} + \frac{M_D}{\tau_{M \rightarrow D}}, \end{aligned} \quad (50)$$

with $M_M(0) = M_0$ and $M_D = 0$. The solution is

$$M_M(t) = M_0 \left(1 - \frac{\mu}{\tau_{D \rightarrow M}} \right) e^{-\mu t} + M_0 \frac{\mu}{\tau_{D \rightarrow M}}. \quad (51)$$

The mean transfer time from the mother to the daughter can be estimated with the following parameters [86]: diffusion

coefficient $D = 6.5 \times 10^{-3} \mu\text{m}^2 \text{s}^{-1}$, a neck length $L = 0.1 \mu\text{m}$, a neck radius $a = 0.2 \mu\text{m}$, a mother radius of $R = 0.9 \mu\text{m}$ and a curvature of $R_c = 0.5 \mu\text{m}$, it is $\tau_{M \rightarrow D} = 5626 \text{ s}$, about an hour and a half.

As shown in figure 24, the connection geometry varies over time, which can change the flux drastically, as formulae (25) indicate. The small transfer rate may lead to an early separation between the mother and daughter cells, prior to reaching the steady state in (51). If steady-state diffusion is reached before separation, the probability density function is uniform in the domain, rendering $M_M(\infty)$ and $M_D(\infty)$ proportional to the respective volumes. In the reduced model (50) the steady-state masses are proportional to the fractions of the residence times in the two cells. In view of (25), these are proportional to the volumes to leading order in small neck radius. The reduced model can be used before steady state is reached. A simple consequence of (51) is that a Brownian simulation of the transferred material (messenger RNA, soluble proteins and so on) has to be run for times $t \gg 1/\mu$ to reach the steady state. Some transitions $M \rightarrow D$ and $D \rightarrow M$ have to occur in the simulation in order for a steady state to set in.

6. Summary and discussion

This review presents recent progress in molecular-level stochastic modeling and analysis in cellular biology. The main feature in the reviewed models is the transition from the molecular to the cellular time scale. Rare events on the molecular time scale, such as passage through narrow openings and finding hidden targets, are the determinants of the time scale of cell function and its regulation. The main thrust of the new analysis of these models is the coarse-graining of molecular-level Brownian motion in biological cells or on their membranes into the cellular time scale, where cell function can be discerned. The key factor in this coarse-graining is the identification of the NET as the determinant of the coarse time scale and its analytical evaluation. The coarse-grained models are used to analyze and simulate subcellular processes, to quantify their biological functions, and to be used for data analysis.

The reviewed methods of modeling and analysis can be extended in several directions. These include the incorporation of electrical interactions on the molecular level, which lead

to the Poisson–Nernst–Planck equations [3] for the densities of the different charged species. The NET problem in this situation is much harder, though not impossible. It determines the time scale of electrical signaling in synapses and introduces hard nonlinearity into the density–voltage characteristic. Another extension of the present modeling and analysis is in the theory of threshold in chemical reactions, which can be used to quantify checkpoints processes in biology, such as the induction of plasticity [59], the decision to start spindle separation during cell replication [60] or any other decision process that occurs when a certain amount of molecules are activated. Still another direction is the modeling of virus trafficking, which can be extended to enveloped viruses. Other steps of viral infection should be further modeled, such as the insertion of the genetic material to a DNA site, the synthesis part, the formation of the capsid and budding. Another example is the search for a promoter site in the cell nucleus. Indeed, a key feature in the search by a transcription factor is the local structure of the DNA conformation and chromatin near the specific binding site. There are no modeling approaches so far that have integrated the DNA organization in the estimation of the expected time to find the DNA promoter site. It would be interesting to combine polymer dynamics in microdomains with the narrow escape theory. Finally, our approach to model synaptic transmission could be extended to include various molecular feedbacks implied in modulating the probability of vesicular release.

Acknowledgment

This research of D Holcman is supported by an ERC-starting Grant.

Appendix

In this appendix, we present the derivation for the NET and a simple version of the Dire Strait in dimension 2. While the first derivations is based on the use of the Neumann–Green’s functions [57], the second relies on Möbius conformal mapping [51].

A.1. Derivation of the asymptotic formula for the NET

Equation (3) is an elliptic partial differential equation with mixed Dirichlet–Neumann boundary value condition for the Laplace operator in a bounded domain $\Omega \subset \mathbb{R}^d$ ($d = 2, 3$) with absorbing boundary on $\partial\Omega_a$. The averaged NET is given by

$$\bar{\tau} = \frac{1}{|\Omega|} \int_{\Omega} u(x) dx. \quad (52)$$

The compatibility condition, obtained integrating equation (3), is

$$\int_{\partial\Omega_a} \frac{\partial u(x)}{\partial \nu_x} dS_x = -\frac{|\Omega|}{D}. \quad (53)$$

The NET is also associated with the principal eigenvalue λ_1 of the mixed Dirichlet–Neumann problem for the Laplace equation in Ω , whose Dirichlet boundary $\partial\Omega_a$ is only a

small patch on the otherwise Neumann boundary $\partial\Omega_r$, is asymptotically the reciprocal of the NET $\bar{\tau}$ in the limit of shrinking patch size [38, 44]. That is,

$$\lambda_1 \sim \frac{1}{\bar{\tau}} \quad \text{for } \frac{|\partial\Omega_a|}{|\partial\Omega_r|} \ll 1.$$

The solution can be represented [44, 57] in terms of the boundary flux $\partial u(x)/\partial \nu$ and the Neumann function $N(x, y)$ of Ω . For a bounded domain $\Omega \subset \mathbb{R}^3$

$$\nabla_x^2 N(x, y) = -\delta(x - y) + \frac{1}{|\Omega|}, \quad \text{for } x, y \in \Omega \quad (54)$$

$$\frac{\partial N(x, y)}{\partial \nu_x} = 0, \quad \text{for } x \in \partial\Omega, y \in \Omega.$$

For $z \in \partial\Omega$, $y \in \Omega \cup \partial\Omega$, the singularity of the Neumann function (in dimensionless variables) is

$$N(y, z) = \begin{cases} \frac{1}{2\pi|y-z|} - \frac{[L(z)+N(z)]}{8\pi} \log|y-z| + v_S(y, z) & \text{in 3D} \\ -\frac{1}{2\pi} \log|y-z| + v_S(y, z), & \text{in 2D} \end{cases}$$

where $L(z)$ and $N(z)$ are the principal curvatures of $\partial\Omega$ at z and $v_S(y, z)$ is a bounded function of x, y in Ω [57].

A.2. The Helmholtz integral equation

The NET is found by solving an integral equation. In fact, when $\partial\Omega_a$ is a disk of radius a , such that $\varepsilon = a/|\Omega|^{1/3} \ll 1$, the non-vanishing boundary flux is $g(x) = \frac{\partial u(x)}{\partial \nu_x}$ for $x \in \partial\Omega_a$. Green’s identity applied to u (equation (3)) and the Green’s function (55) give to leading order in ε [57] that for $y \in \partial\Omega_a$,

$$\int_{\partial\Omega_a} N(x, y) g(x) dS_x = \frac{1}{|\Omega|} \int_{\Omega} u(x) dx = -C \rightarrow \infty \quad \text{as } \varepsilon \rightarrow 0.$$

The singularity of $N(x, y)$ gives for $y \in \partial\Omega_a$ the generalized Helmholtz equation

$$\int_{\partial\Omega_a} g(x) \left[\frac{1}{2\pi|x-y|} + H(x, y) \log|x-y| + O(1) \right] dS_x = -C,$$

where for $x, y \in \partial\Omega_a$ and $\varepsilon \ll 1$

$$H(x, y) = -\frac{1}{8\pi} [L(y) + N(y)] \sim -\frac{1}{8\pi} [L(\mathbf{0}) + N(\mathbf{0})].$$

To construct the solution, we expand the flux as

$$g(x) = g_0(x) + g_1(x) + g_2(x) + \dots, \quad (55)$$

where $g_{i+1}(x) \ll g_i(x)$ for $\varepsilon \rightarrow 0$ and choose $g_0(x) = -2C/a\pi\sqrt{1-|x|^2/a^2}$ [89]

If $\partial\Omega_a$ is a circular disk of radius a , then

$$\frac{1}{2\pi} \int_{\partial\Omega_a} \frac{g_0(x)}{|x-y|} dS_x = C \quad \text{for all } y \in \partial\Omega_a.$$

It follows that $g_1(x)$ satisfies the integral equation

$$\frac{1}{2\pi} \int_{\partial\Omega_a} \frac{g_1(x)}{|x-y|} dS_x = \frac{2C}{a\pi} \int_{\partial\Omega_a} \frac{H(x, y) \log|x-y|}{\sqrt{1-\frac{|x|^2}{a^2}}} dS_x.$$

Setting $y = a\eta$, $x = a\xi$, we obtain in polar coordinates

$$\begin{aligned} & \frac{1}{2\pi} \int_{\partial\Omega_a} \frac{g_1(x)}{|x-y|} dS_x \\ &= \frac{2Ca^2}{a\pi} \int_0^{2\pi} d\theta \int_0^1 \frac{H(a\xi, a\eta) [\log a + \log |\xi - \eta|]}{\sqrt{1-r^2}} r dr. \end{aligned}$$

The second term in the expansion of the NET is found from the expansion (55) in the limit $\varepsilon \rightarrow 0$ (e.g. keeping $|\Omega|$ fixed and $a \rightarrow 0$), from the equation

$$\begin{aligned} & \frac{1}{2\pi} \int_{\partial\Omega_a} \frac{g_1(x)}{|x-y|} dS_x \\ &= -\frac{C[L(\mathbf{0}) + N(\mathbf{0})]}{2\pi} a \log a + o(a \log a). \end{aligned}$$

The solution is $g_1(x) = -C[L(\mathbf{0}) + N(\mathbf{0})]/\pi^2 \sqrt{1-|x|^2/a^2} \log a + o(\log a)$. Finally, to determine the asymptotic value of C , we recall that $g(x) = \frac{\partial u(x)}{\partial \nu_x}$ and use in the compatibility condition. Finally, the approximation

$$\begin{aligned} g(x) &\sim g_0(x) + g_1(x) \\ &\sim \frac{-2C}{a\pi \sqrt{1-\frac{|x|^2}{a^2}}} \left[1 + \frac{L(\mathbf{0}) + N(\mathbf{0})}{2\pi} a \log a \right]. \end{aligned}$$

We obtain the NET $\bar{\tau} = C$ as

$$\bar{\tau} = \frac{|\Omega|}{4aD \left[1 + \frac{L(\mathbf{0})+N(\mathbf{0})}{2\pi} a \log a + o(a \log a) \right]} \quad (56)$$

(see also for further details [57]).

The formula is also true for Riemannian manifolds [44]. The constant term in the NET expansion can be explicitly computed on the disk and the three-dimensional ball [42]. This term allows one to study the interaction between many small absorbing holes [42], see also [90, 91]. Precise information about the boundary layer near the absorbing window are given in [45].

A.3. Asymptotics by conformal mapping

For cusp geometry the singularity of Green's function may not be the dominant contributor to the MFPT. Furthermore, the method of matched asymptotic expansions, used in [38–40, 42] for calculating the MFPT to the interface on a smooth boundary, requires major modifications for an interface at the end of a bottleneck, because the boundary layer problem does not reduce to the classical electrified disk problem [89]. Altogether different boundaries or internal layers at absorbing windows located at the end of a cusp-like funnel are needed [51]. We present here the derivation of formula (18) for an symmetric cusp.

Consider a Brownian particle in a planar domain Ω with a narrow neck, partially blocked by an obstacle (figure 10), such that the opening in the partially blocked neck is narrow relative to the size of the obstacle. The narrow passage can be described locally as the narrow neck formed by two tangent circles that are moved slightly apart. The domain Ω is enclosed by an arc of a circle of radius R and two arcs of circles of radius 1, as shown in figure 8. Scaling space with the radius of the smaller circle changes the dimension of the diffusion coefficient D to

that of frequency. The two arcs are removed from each other by a dimensionless distance $\varepsilon \ll 1 < R$, form a narrow passage.

The MFPT $\bar{\tau}$ of a Brownian particle with diffusion coefficient D from a point $(x, y) \in \Omega$ to the short black segment $\partial\Omega_a$ in figure 8 is the solution of the boundary value problem (3). We construct an asymptotic solution for small gap ε by first mapping the domain Ω in figure 8 conformally into its image under the Möbius transformation of the two bounding circles (thin line) into concentric circles. We put the origin of the complex plane $z = x + iy$ at the center of the right upper circle and set

$$w(z) = \frac{z - \alpha}{1 - \alpha z}, \quad (57)$$

where

$$\alpha = \frac{(-2 - \varepsilon \pm \sqrt{4\varepsilon + \varepsilon^2})}{2} = -1 \pm \sqrt{\varepsilon} + O(\varepsilon), \quad (58)$$

which maps the right upper circle into itself and Ω is mapped onto the domain $\Omega_w = w(\Omega)$ in figure 8 (left). The straits in figure 8 (right) are mapped onto the ring enclosed between the green and red circular arcs and the large disk is mapped onto the small red disk with the large red arc mapped onto the small blue arc. The radius of the small red disk and the elevation of its center above the real axis are $O(\sqrt{\varepsilon})$. The short black segment (of length ε) is mapped onto the thick black segment (of length $2\sqrt{\varepsilon} + O(\varepsilon)$) (figure 25).

Setting $u(z) = v(w)$, equation (3) is converted into

$$\begin{aligned} \nabla_w^2 v(w) &= -\frac{1}{D|w'(z)|^2} = -\frac{4\varepsilon + O(\varepsilon^{3/2})}{D|w(1 - \sqrt{\varepsilon}) - 1 + O(\varepsilon)|^4} \\ &\quad \text{for } w \in \Omega_w \\ \frac{\partial v(w)}{\partial n} &= 0 \quad \text{for } w \in \partial\Omega_w - \partial\Omega_{w,a} \\ v(w) &= 0 \quad \text{for } w \in \partial\Omega_{w,a}. \end{aligned} \quad (59)$$

The MFPT is bounded above and below by that from the inverse image of a circular ring cut by lines through the origin, tangent to the red disk at polar angles $\theta = c_1\sqrt{\varepsilon}$ (brown) and $\theta = c_2\sqrt{\varepsilon}$ (cyan) for some positive constants c_1, c_2 , independent of ε (see figure 8 (left)). Therefore, the MFPT from Ω equals that from the inverse image of a ring cut by an intermediate angle $\theta = c\sqrt{\varepsilon}$ (black).

The solution of the boundary value problem (59) is to leading order independent of the radial variable in polar coordinates $w = re^{i\theta}$. Fixing $r = 1$, we impose the reflecting boundary condition at $\theta = c\sqrt{\varepsilon}$, where $c = O(1)$ is a constant independent of ε to leading order, and the absorbing condition at $\theta = \pi$. Thus, we obtain the leading order approximation

$$\begin{aligned} v(e^{i\theta}) &= \frac{4\varepsilon}{D} \int_{\theta}^{\pi} d\varphi \int_{c\sqrt{\varepsilon}}^{\varphi} \frac{d\eta}{|e^{i\eta} - 1 - e^{i\eta}\sqrt{\varepsilon}|^4} \\ &= \frac{4\varepsilon}{D} \int_{c\sqrt{\varepsilon}}^{\pi} \frac{(\pi - \eta) d\eta}{|e^{i\eta} - 1 - e^{i\eta}\sqrt{\varepsilon}|^4}. \end{aligned} \quad (60)$$

We evaluate asymptotically the integrals

$$\begin{aligned} \frac{4\varepsilon}{D} \int_{c\sqrt{\varepsilon}}^{\pi} \frac{\eta d\eta}{|e^{i\eta} - 1 - e^{i\eta}\sqrt{\varepsilon}|^4} &= \frac{4}{D} \int_c^{\pi/\sqrt{\varepsilon}} \frac{\zeta d\zeta}{|1 + \zeta^2 + O(\varepsilon\zeta^2)|^2} \\ &= \frac{4}{D(c+1)} (1 + O(\sqrt{\varepsilon})). \end{aligned}$$

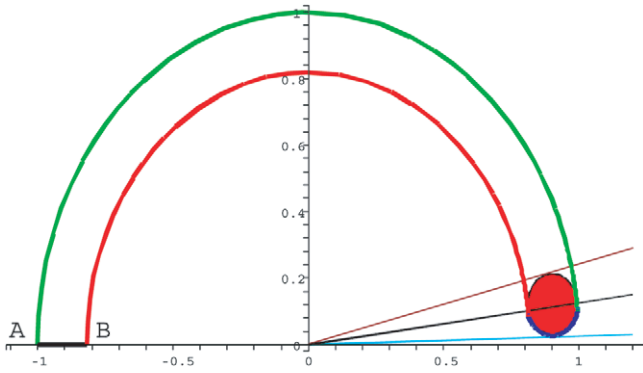


Figure 25. The image $\Omega_w = w(\Omega)$ of the domain in figure 8 (marked Ω' in dimensionless variables) under the conformal mapping (57). The straits leading to the narrow passage AB in Ω are mapped onto the ring enclosed between the green and red circular arcs and the large disk is mapped onto the small red disk with the large red arc mapped onto the small blue arc. The segment AB (of length ε) is mapped onto the thick black segment (of length $2\sqrt{\varepsilon} + O(\varepsilon)$).

and

$$\begin{aligned} \frac{4\varepsilon}{D} \int_{c\sqrt{\varepsilon}}^{\pi} \frac{d\eta}{|e^{i\eta} - 1 - e^{i\eta}\sqrt{\varepsilon}|^4} &= \frac{4}{D\sqrt{\varepsilon}} \int_c^{\pi/\sqrt{\varepsilon}} \frac{d\zeta}{|1 + \zeta^2 + O(\varepsilon\zeta^2)|^2} \\ &= \frac{4C}{D\sqrt{\varepsilon}} (1 + O(\sqrt{\varepsilon})), \end{aligned}$$

where $C = O(1)$ is a constant, so that

$$v(e^{ic\sqrt{\varepsilon}}) = \frac{4\pi C}{D\sqrt{\varepsilon}} (1 + O(\sqrt{\varepsilon})). \quad (61)$$

To determine the value of the constant C , we note that (60) implies that

$$\begin{aligned} \left. \frac{\partial v(e^{i\theta})}{\partial n} \right|_{\partial\Omega_{w,a}} &= \left. \frac{\partial v}{\partial \theta} \right|_{\theta=\pi} = -\frac{4\varepsilon}{D} \int_{c\sqrt{\varepsilon}}^{\pi} \frac{d\eta}{|e^{i\eta} - 1 - e^{i\eta}\sqrt{\varepsilon}|^4} \\ &= -\frac{4C}{D\sqrt{\varepsilon}} (1 + O(\sqrt{\varepsilon})) \end{aligned}$$

and the integration of (59) over Ω_w gives

$$2\sqrt{\varepsilon} \left. \frac{\partial v(e^{i\theta})}{\partial n} \right|_{\partial\Omega_{w,a}} = -\frac{|\Omega|}{D}. \quad (62)$$

Now (62) and (62) imply that $4C = |\Omega|$, so that the MFPT to the straits, $\bar{\tau}$, is

$$\bar{\tau} = \frac{\pi|\Omega|}{2D\sqrt{\varepsilon}} (1 + O(1)) \quad \text{for } \varepsilon \ll |\partial\Omega|. \quad (63)$$

In dimensional variables, the NET (63) is given by

$$\bar{\tau} = \frac{\pi|\Omega|}{2D\sqrt{\varepsilon/R}} \left(1 + O\left(\sqrt{\frac{\varepsilon}{R}}\right) \right), \quad (64)$$

where R is the radius of curvature at the cusp [51, 82, 52].

References

[1] Hille B 2001 *Ion Channels of Excitable Membranes* 3rd edn (Sunderland: Sinauer Associates Inc)

- [2] www.nobelprize.org/nobel_prizes/chemistry/laureates/2003/mackinnon-lecture.html
- [3] Chen D, Lear J and Eisenberg R S 1997 Permeation through an open channel: poisson–Nernst–Planck theory of a synthetic ionic channel *Biophys. J.* **72** 97–116
- [4] Burger M, Eisenberg R S and Engl H W 2007 Inverse problems related to ion channel selectivity *SIAM J. Appl. Math.* **67** 960–89
- [5] Chen D P, Xu L, Tripathy A, Meissner G and Eisenberg R S 1999 Selectivity and permeation in calcium release channel of cardiac muscle: alkali metal ions *Biophys. J.* **76** 1346–66
- Boda D, Nonner W, Valisko M, Henderson D, Eisenberg R S and Gillespie D 2007 Steric selectivity in Na channels arising from protein polarization and mobile side chains *Biophys. J.* **93** 1960–80
- [6] Eisenberg R S and Chen D 1993 Charges, currents, and potentials in ionic channels of one conformation *Biophys. J.* **64** 1405–21
- [7] Aboud, Saraniti S M and Eisenberg R S 2003 Issues in modeling ion transport in biological channels: self-consistent particle-based simulations *J. Comput. Electron.* **2** 239–43
- Im W, Seefeld S and Roux B 2000 A grand canonical Monte Carlo–Brownian dynamics algorithm for simulating ion channels *Biophys. J.* **79** 788–801
- Graf P, Kurnikova M G, Coalson R D and Nitzan A 2004 Comparison of dynamic lattice Monte Carlo simulations and the dielectric self-energy Poisson–Nernst–Planck continuum theory for model ion channels *J. Phys. Chem. B* **108** 2006–15
- [8] Harris K M and Stevens J K 1988 Dendritic spines of rat cerebellar Purkinje cells: serial electron microscopy with reference to their biophysical characteristics *J. Neurosci.* **12** 4455–69
- [9] Bourne J N and Harris K M 2008 Balancing structure and function at hippocampal dendritic spines *Annu. Rev. Neurosci.* **31** 47–67
- [10] Korkotian E, Holcman D and Segal M 2004 Dynamic regulation of spine-dendrite coupling in cultured hippocampal neurons *Euro. J. Neurosci.* **20** 2649–63
- [11] Hotulainen P and Hoogenraad C C 2010 Actin in dendritic spines: connecting dynamics to function *J. Cell Biol.* **189** 619–29
- [12] Newpher T M and Ehlers M D 2009 Spine microdomains for postsynaptic signaling and plasticity *Trends Cell Biol.* **5** 218–27
- [13] Papa M and Segal M 1996 Morphological plasticity in dendritic spines of cultured hippocampal neurons *Neuroscience* **71** 1005–11
- [14] Collin C, Miyaguchi K and Segal M 1997 Dendritic spine density and LTP induction in cultured hippocampal slices *J. Neurophysiol.* **77** 1614–23
- [15] Korkotian E and Segal M 1999 Release of calcium from stores alters the morphology of dendritic spines in cultured hippocampal neurons *Proc. Natl Acad. Sci. USA* **96** 12068–72
- [16] Svoboda K, Tank D W and Denk W 1996 Direct measurement of coupling between dendritic spines and shafts *Science* **272** 716–9
- [17] Bloodgood B L and Sabatini B L 2005 Neuronal activity regulates diffusion across the neck of dendritic spines *Science* **310** 866–9
- [18] Holcman D, Marchewka A and Schuss Z 2005 Survival probability of diffusion with trapping in cellular neurobiology *Phys. Rev. E* **72** 031910
- [19] Holcman D, Korkotian E and Segal M 2005 Calcium dynamics in dendritic spines, modeling and experiments *Cell Calcium* **37** 467–75

- [20] Biess A, Korkotian E and Holcman D 2007 Diffusion in a dendritic spine: the role of geometry *Phys. Rev. E* **76** 021922
- [21] Holcman D and Kupka I 2010 Some questions in computational cellular biology *J. Fixed Point Theory Appl.* **7** 67–83
- [22] Chen L, Chetkovich D M, Petralia R S, Sweeney N T, Kawasaki Y, Wenthold R J, Brecht D S and Nicoll R A 2000 Stargazin regulates synaptic targeting of AMPA receptors by two distinct mechanisms *Nature* **408** 936
- [23] Brecht D S and Nicoll R A 2003 AMPA receptor trafficking at excitatory synapses *Neuron* **40** 361
- [24] Adesnik H, Nicoll R A and England P M 2005 Photoinactivation of native AMPA receptors reveals their real-time trafficking *Neuron* **48** 977–85
- [25] Shi S H, Hayashi Y, Petralia R S, Zaman S H, Wenthold R J, Svoboda K and Malinow R 1999 Rapid spine delivery and redistribution of AMPA receptors after synaptic NMDA receptor activation *Science* **284** 1811–6
- [26] Malinow R and Malenka R C 2002 AMPA receptor trafficking and synaptic plasticity *Annu. Rev. Neurosci.* **25** 103–26
- [27] Malinow R 2003 AMPA receptor trafficking and long-term potentiation *Philos. Trans. R. Soc. Lond. B* **358** 707–14
- [28] Earnshaw B A and Bressloff P C 2006 A biophysical model of AMPA receptor trafficking and its regulation during LTP/LTD *J. Neurosci.* **26** 12362–73
- [29] Holcman D and Triller A 2006 Modeling synaptic dynamics and receptor trafficking *Biophys. J.* **91** 2405–15
- [30] Ashby M C, Maier S R, Nishimune A and Henley J M 2006 Lateral diffusion drives constitutive exchange of AMPA receptors at dendritic spines and is regulated by spine morphology *J. Neurosci.* **26** 7046
- [31] Bressloff P C and Newby J M 2013 *Stochastic Models of Intracellular Transport* OCCAM Preprint Number 12/45, University of Oxford, UK (2012) and *Rev. Mod. Phys.* **85** 135–96
- [32] Manley S, Gillette J M, Patterson G H, Shroff H, Hess H F, Betzig E and Lippincott-Schwartz J 2008 High-density mapping of single-molecule trajectories with photoactivated localization microscopy *Nature Methods* **5** 155
- [33] Huang B, Babcock H and Zhuang X 2010 Breaking the diffraction barrier: super-resolution imaging of cells *Cell* **143** 1047–58
- [34] Schuss Z 2010 Equilibrium and recrossings of the transition state: what can be learned from diffusion? *J. Phys. Chem. C* **114** 20320–34
- [35] Pontryagin L S, Andronov A A and Vitt A A 1933 On the statistical treatment of dynamical systems *J. Theor. Exper. Phys. (Russ)* **3** 165–80
- [36] Pontryagin L S, Andronov A A and Vitt A A 1989 On the statistical treatment of dynamical systems *Noise Nonlinear Dyn.* **1** 329–40
- [37] Schuss Z 2010 *Diffusion and Stochastic Processes: an Analytical Approach* (New York: Springer)
- [38] Ward M J and Keller J B 1993 Strong localized perturbations of eigenvalue problems *SIAM J. Appl. Math.* **53** 770–98
- [39] Ward M J, Henshaw W D and Keller J B 1993 Summing logarithmic expansions for singularly perturbed eigenvalue problems *SIAM J. Appl. Math.* **53** 799–828
- [40] Ward M J and Van De Velde E 1992 The onset of thermal runaway in partially insulated or cooled reactors *IMA J. Appl. Math.* **48** 53–85
- [41] Kolokolnikov T, Titcombe M and Ward M J 2005 Optimizing the fundamental Neumann eigenvalue for the Laplacian in a domain with small traps *Eur. J. Appl. Math.* **16** 161–200
- [42] Cheviakov A, Ward M J and Straube R 2010 An asymptotic analysis of the mean first passage time for narrow escape problems: II. The sphere *SIAM Multiscale Modeling Simul.* **8** 836–70
- [43] Holcman D and Schuss Z 2004 Escape through a small opening: receptor trafficking in a synaptic membrane *J. Stat. Phys.* **117** 191–230
- [44] Singer A, Schuss Z, Holcman D and Eisenberg B 2006 Narrow escape I *J. Stat. Phys.* **122** 437–63
- [45] Singer A, Schuss Z and Holcman D 2006 Narrow escape II *J. Stat. Phys.* **122** 465–89
- [46] Singer A, Schuss Z and Holcman D 2006 Narrow escape III *J. Stat. Phys.* **122** 491–509
- [47] Gandolfi A, Gerardi A and Marchetti F 1985 Diffusion-controlled reactions in two dimensions *Acta Applicandae Math.* **4** 139–59
- [48] Linderman J and Laufengerger D 1986 Analysis of intracellular receptor/Ligand sorting: calculation of mean surface and bulk diffusion times within a sphere *Biophys. J.* **50** 295–305
- [49] Coombs D, Straube R and Ward M 2009 Diffusion on a sphere with localized traps: mean first passage time, eigenvalue asymptotics, and Fekete points *SIAM J. Appl. Math.* **70** 302–32
- [50] Schuss Z, Singer A and Holcman D 2007 The narrow escape problem for diffusion in cellular microdomains *Proc. Natl Acad. Sci. USA* **104** 16098–103
- [51] Holcman D and Schuss Z 2012 Brownian motion in dire straits: I *SIAM Multiscale Modeling Simul.* **10** 1204–31
- [52] Holcman D, Hoze N and Schuss Z 2011 Narrow escape through a funnel and effective diffusion on a crowded membrane *Phys. Rev. E* **84** 021906
- [53] Holcman D and Schuss Z 2005 Stochastic chemical reactions in microdomains *J. Chem. Phys.* **122** 114710
- [54] Bressloff P C and Earnshaw B A 2009 A dynamical corral model of protein trafficking in spines *Biophys. J.* **96** 1786–802
- [55] Holcman D and Schuss Z 2011 Diffusion laws in dendritic spines *J. Math. Neurosci.* **1** 10
- [56] Singer A and Schuss Z 2007 Activation through a narrow opening *SIAM J. Appl. Math.* **68** 98–108
- [57] Singer A, Schuss Z and Holcman D 2008 Narrow escape and leakage of Brownian particles *Phys. Rev. E* **78** 051111
- [58] Reingruber J and Holcman D 2011 The narrow escape problem in a flat cylindrical microdomain with application to diffusion in the synaptic cleft *Multiscale Modeling Simul.* **9** 2 793–816
- [59] Dao Duc K and Holcman D 2010 Threshold activation for stochastic chemical reactions in microdomains *Phys. Rev. E* **81** 041107
- [60] Dao Duc K and Holcman D 2012 Using default constraints of the spindle assembly checkpoints to estimate the associate chemical rates *BMC Biophys.* **5** 1
- [61] Taflia A and Holcman D 2011 Estimating the synaptic current in a multiconductance AMPA receptor model *Biophys. J.* **101** 781–92
- [62] Freche D, Pannasch U, Rouach N and Holcman D 2011 Synapse geometry and receptor dynamics modulate synaptic strength *PLoS One* **6** e25122
- [63] Südhof T C 2008 Neurotrophins and neurexins link synaptic function to cognitive disease *Nature* **455** 903–11
- [64] Durand C M, Perroy J, Loll F, Perrais D, Fagni L, Bourgeron T, Montcouquiol M and Sans N 2011 SHANK3 mutations identified in autism lead to modification of dendritic spine morphology via an actin-dependent mechanism *Mol. Psychiatry* **17** 71–84
- [65] Dalva M B, McClelland A C and Kayser M S 2007 Cell adhesion molecules: signalling functions at the synapse *Nature Rev. Neurosci.* **8** 206–20

- [66] Futai K *et al* 2007 Retrograde modulation of presynaptic release probability through signaling mediated by PSD-95-neurologin *Nature Neurosci.* **10** 186–95
- [67] Kusumi A, Sako Y and Yamamoto M 1993 *Biophys. J.* **65** 2021
- [68] Kusumi A *et al* 2005 *Annu. Rev. Biophys. Biomol. Struct.* **34** 351
- [69] Edidin M, Kuo S C and Sheetz M P 1991 *Science* **254** 1379
- [70] Sheetz M P 1993 Glycoprotein motility and dynamic domains in fluid plasma membranes. *Ann. Rev. Biophys. Biomol. Struct.* **22** 417
- [71] Suzuki K and Sheetz M P 2001 Binding of cross-linked glycosylphosphatidylinositol-anchored proteins to discrete actin-associated sites and cholesterol-dependent domains *Biophys. J.* **81** 2181
- [72] Saxton M J 1993 Lateral diffusion in an archipelago. Dependence on tracer size *Biophys. J.* **64** 1766
- [73] Saxton M J 1995 Single-particle tracking: effects of corrals *Biophys. J.* **69** 389
- [74] Saxton M J and Jacobson K 1997 Single-particle tracking: applications to membrane dynamics *Annu. Rev. Biophys. Biomol. Struct.* **26** 373
- [75] Renner M, Choquet D and Triller A 2009 Control of the postsynaptic membrane viscosity *J. Neurosci.* **29** 2926–37
- [76] Saffman P G and Delbrück M 1975 Brownian motion in biological membranes *Proc. Natl Acad. Sci.* **72** 3111–3
- [77] Schuss Z 1980 *Theory and Applications of Stochastic Differential Equations* (New York: Wiley)
- [78] Choquet D and Triller A 2003 The role of receptor diffusion in the organization of the postsynaptic membrane *Nature Rev. Neurosci.* **4** 251–65
- [79] Lieber A, Leis A, Kushmaro A, Minsky A and Medalia O 2009 Chromatin organization and radio resistance in the bacterium *Gemmata obscuriglobus* *J. Bacteriol.* **191** 1439–45
- [80] Minsky A 2004 *Annu. Rev. Biophys. Biomol. Struct.* **33** 317–42
- [81] Levin-Zaidman S, Englander J, Shimoni E, Sharma A K, Minton K W and Minsky A 2003 *Science* **299** 254–6
- [82] Holcman D and Schuss Z 2012 Brownian needle in dire straits: stochastic motion of a rod in very confined narrow domains *Phys. Rev. E* **85** 010103(R)
- [83] Macheboeuf P, Di Guilmi A M, Job V, Vernet T, Dideberg O and Dessen A 2005 Active site restructuring regulates ligand recognition in class A penicillin-binding proteins *Proc. Natl Acad. Sci. USA* **102** 577–82
- [84] Reingruber J and Holcman D 2009 The gated narrow escape time for molecular signaling *Phys. Rev. Lett.* **103** 148102
- [85] Doering C 2000 *Stochastic Processes in Physics, Chemistry, and Biology (Lecture Notes in Physics)* vol 557 (Berlin: Springer) p 316
- [86] Gehlen L R, Nagai S, Shimada K, Meister P, Taddei A and Gasser S M 2011 Nuclear geometry and rapid mitosis ensure asymmetric episome segregation in yeast *Curr. Biol.* **21** 25–33
- [87] Filkova E and Delay R J 1982 Cytoplasmic actin in dendritic spines as a possible mediator of synaptic plasticity *J. Cell Biol.* **95** 350–65
- [88] Tsaneva K, Burgo A, Galli T and Holcman D 2009 Quantifying neurite growth mediated by interactions between secretory vesicles, microtubules and actin networks *Biophys. J.* **96** 840–57
- [89] Crank J 1980 *The Mathematics of Diffusion* 2nd edn (Oxford: Oxford University Press)
- [90] Holcman D and Schuss Z 2008 The first eigenvalue of Laplace operator with small holes *J. Phys. A: Math. Theor.* **41** 155001
- [91] Holcman D and Schuss Z 2008 Diffusion through a cluster of small windows and flux regulation in microdomains *Phys. Lett. A* **372** 3768–72